Advances in Applied Mathematics and Mechanics
Adv. Appl. Math. Mech., Vol. **15**, No. 6, pp. 1562-1601

DOI: 10.4208/aamm.OA-2021-0270
December 2023

A Node-Based Smoothed Finite Element Method with Linear Gradient Fields for Elastic Obstacle Scattering Problems

Junhong Yue[1,*], Yu Wang[2], Yan Li[3] and Ming Li[2]

[1] *College of Data Science, Taiyuan University of Technology, Taiyuan, Shanxi 030024, China*
[2] *College of Mathematics, Taiyuan University of Technology, Taiyuan, Shanxi 030024, China*
[3] *School of Mechanics and Engineering, Southwest Jiaotong University, Chengdu, Sichuan 611731, China*

Received 19 August 2021; Accepted (in revised version) 3 November 2022

Abstract. In this paper, a node-based smoothed finite element method (NS-FEM) with linear gradient fields (NS-FEM-L) is presented to solve elastic wave scattering by a rigid obstacle. By using Helmholtz decomposition, the problem is transformed into a boundary value problem with coupled boundary conditions. In numerical analysis, the perfectly matched layer (PML) and transparent boundary condition (TBC) are introduced to truncate the unbounded domain. Then, a linear gradient is constructed in a node-based smoothing domain (N-SD) by using a complete order of polynomial. The unknown coefficients of the smoothed linear gradient function can be solved by three linearly independent weight functions. Further, based on the weakened weak formulation, a system of linear equation with the smoothed gradient is established for NS-FEM-L with PML or TBC. Some numerical examples also demonstrate that the presented method possesses more stability and high accuracy. It turns out that the modified gradient makes the NS-FEM-L-PML and NS-FEM-L-TBC possess an ideal stiffness matrix, which effectively overcomes the instability of original NS-FEM. Moreover, the convergence rates of L^2 and H^1 semi-norm errors for the two NS-FEM-L models are also higher.

AMS subject classifications: 35L05, 65N99

Key words: Elastic obstacle scattering, Helmholtz equations, perfectly matched layer, transparent boundary condition, NS-FEM with linear gradient.

---

*Corresponding author.
Email: yuejunhong@tyut.edu.cn (J. Yue)

1 Introduction

The obstacle scattering [1] has been widely used in medicine, location detection and other fields. It can be divided into acoustic, electromagnetic and elastic scattering. These problems have been widely studied in theoretical [2–4] and numerical [5,6] aspects.

A fundamental difficulty in the obstacle scattering is that the problem domain is open. Hence some techniques need to be applied to make the problem domain truncated. At present, there are many techniques have been studied, among which the common ones include perfectly matched layer (PML) [7], transparent boundary condition (TBC) [3]. The PML refers to the method of applying a layer with a special absorption medium layer to a certain domain around the obstacle, so that the wave can be fully absorbed upon reaching the outer boundary of PML. Many researchers have proved that PML is a valid method and is widely used in solving acoustic wave [8–11], elastic wave [12–16] and electromagnetic wave scattering [4,7]. The TBC is also a common technique, which is constructed using the analytic solutions with an infinite Fourier series. By imposing the TBC on the boundary of the truncated domain, the reflection of the wave can be avoided. The TBC has been used for solving many wave scattering problems [17–24].

Both compressional wave and shear wave exist in the scattering of elastic waves, which makes the study of elastic waves more complicated and it is not easy to obtain analytical solutions for arbitrarily shaped obstacles. Currently, many discrete numerical methods are proposed for solving these problems, such as the boundary integral method [1], finite element method (FEM) [25,26], smoothed point interpolation method (S-PIM) [27], and smoothed finite element method (S-FEM) [28]. Since PML and TBC are artificial boundary conditions in nature, there will be certain errors when they are applied. Usually, due to the over-stiff property of FEM, the solution accuracy of FEM model with the TBC or PML is not very high for solving this problem. In order to make up for this deficiency of FEM, Liu et al. proposed the G space theory based on weakened weak (W2) formulations and constructed S-FEM models [29,30]. Besides, according to different type of smoothing domains, the S-FEM can be divided into the cell-based S-FEM (CS-FEM), the node-based S-FEM (NS-FEM), the edge-based S-FEM (ES-FEM) in 2D problem. These models can obtain high precision solutions for different problems, such as solid mechanics problems [31–33], thermal problems [34] and so on. Recently, Yue and Wu proposed ES-FEM model with PML technique [5] and TBC technique [35] for solving elastic wave obstacle scattering, respectively. The NS-FEM has been proved to have many properties for solid mechanics, such as, spatial discrete stability, time response stability and possessing near-accurate stiffness and so on [36,37]. But we noticed that the original NS-FEM cannot be extended to wave scattering problems due to the "over-soft" stiffness of the method. Chai first presented a stable NS-FEM (SNS-FEM) for the analysis of acoustic scattering to cure the instability of original NS-FEM [23], and Wang solved the elastic wave obstacle scattering problem by using SNS-FEM and PML technique [38]. In addition, Liu proposed a novel pick-out technique for constructing higher order smoothed derivatives [39]. Li and Liu also extended this technique to NS-FEM (NS-FEM-L), which have been employed to solve the static, free and force vibration analyses of solid [40], and contact problems [41]. Therefore, we expect that the NS-FEM-L can also be used for improving the accuracy of FEM solutions and the instability of original NS-FEM.

In this paper, the NS-FEM-L models combine PML and TBC techniques for solving the elastic wave obstacle scattering. The scattering model, PML and TBC truncation techniques are given in next section. In Section 3, the NS-FEM is introduced and the linear gradient field is constructed on the node-based SD using the three linearly independent weight functions, which further forms the modified smoothed gradient matrix. Section 4 derives the formulations of NS-FEM-L with PML and TBC by using the modified smoothed gradient matrix in detail. Different numerical examples are carried out to study the convergence and stability of the proposed method in Section 5. Some conclusions are made in Section 6.

2 Basic equations for elastic scattering problem by an obstacle

Consider a time-harmonic plane elastic wave scattering problem by a rigid obstacle D, where the obstacle boundary is Γ_D. The scattering problem domain outside the obstacle is denoted by $\Omega=\mathbb{R}^2\setminus\overline{D}$, as shown in Fig. 1. For the plane elastic wave obstacle scattering, the total field $\boldsymbol{u}=(u_1,u_2)$ satisfies the following Navier equation

$$\mu\Delta\boldsymbol{u}+(\lambda+\mu)\nabla\nabla\cdot\boldsymbol{u}+\omega^2\boldsymbol{u}=0 \quad \text{in } \Omega, \tag{2.1}$$

where λ and μ are the Lame constants satisfying $\mu>0$ and $\lambda+\mu>0$; $\omega>0$ is the angular frequency. It is well known that the total field is the superposition of incident and scattered field, i.e., $\boldsymbol{u}=\boldsymbol{u}^{inc}+\boldsymbol{v}$, and an incident plane elastic wave also satisfies the Navier equation, so we can get the scattered field $\boldsymbol{v}=(v_1,v_2)$ satisfies

$$\mu\Delta\boldsymbol{v}+(\lambda+\mu)\nabla\nabla\cdot\boldsymbol{v}+\omega^2\boldsymbol{v}=0 \quad \text{in } \Omega. \tag{2.2}$$

Since the obstacle is rigid, the obstacle boundary condition for scattered field is

$$\boldsymbol{v}=-\boldsymbol{u}^{inc} \quad \text{on } \Gamma_D. \tag{2.3}$$

In addition, the scattered field $\boldsymbol{v}$ is required to satisfy the Kupradze Sommerfeld radiation condition

$$\lim_{\rho\to\infty}\rho^{\frac{1}{2}}(\partial_\rho\boldsymbol{v}_p-\mathrm{i}\kappa_p\boldsymbol{v}_p)=0, \quad \lim_{\rho\to\infty}\rho^{\frac{1}{2}}(\partial_\rho\boldsymbol{v}_s-\mathrm{i}\kappa_s\boldsymbol{v}_s)=0, \quad \rho=|\mathbf{x}|, \tag{2.4}$$

where $\boldsymbol{v}_p:=-\kappa_p^{-2}\nabla\nabla\cdot\boldsymbol{v}$, $\boldsymbol{v}_s:=\kappa_s^{-2}\mathbf{curl}\,curl\boldsymbol{v}$ are the compressional part and the shear part, respectively, and $\kappa_p=\omega/\sqrt{\lambda+2\mu}$, $\kappa_s=\omega/\sqrt{\mu}$, $curl\boldsymbol{v}=\partial_x v_2-\partial_y v_1$, $\mathbf{curl}\psi=[\partial_y\psi-\partial_x\psi]^{\mathrm{T}}$.

For any solution $\boldsymbol{v}$ of Eq. (2.2), it is decomposed into the compressional and shear parts by using the Helmholtz decomposition:

$$\boldsymbol{v}=\nabla\phi+\mathbf{curl}\psi, \tag{2.5}$$

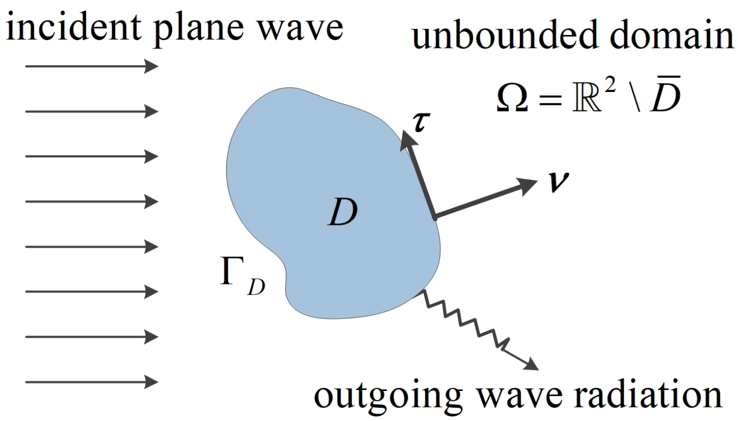

Figure 1: The problem geometry of elastic scattering by an arbitrary obstacle.

where ϕ and ψ are scalar potentials, which are called Lame potential. Substituting Eq. (2.5) into Eq. (2.2) gives

$$\nabla\left((\lambda+2\mu))\Delta\phi+\omega^2\phi\right)+\mathbf{curl}\left(\mu\Delta\psi+\omega^2\psi\right)=0,$$

which is fulfilled if ϕ and ψ satisfy the Helmholtz equations

$$\Delta\phi+\kappa_p^2\phi=0, \quad \Delta\psi+\kappa_s^2\psi=0 \quad \text{in } \Omega, \tag{2.6}$$

where κ_p and κ_s are the compressional and shear wavenumbers, respectively. The boundary condition by using Helmholtz decomposition (2.5) becomes

$$\partial_\nu\phi+\partial_\tau\psi=f, \quad \partial_\nu\psi-\partial_\tau\phi=g \quad \text{on } \Gamma_D, \tag{2.7}$$

where $f=-\boldsymbol{\nu}\cdot\boldsymbol{u}^{inc}$, $g=\boldsymbol{\tau}\cdot\boldsymbol{u}^{inc}$. $\boldsymbol{\nu}=(\nu_1,\nu_2)^{\mathrm{T}}$ and $\tau=(\tau_1,\tau_2)^{\mathrm{T}}$ denote unit normal and tangential vectors on Γ_D, and satisfy $\tau_1=-\nu_2$, $\tau_2=\nu_1$, as shown in Fig. 1.

The potentials need to satisfy the Sommerfeld radiation condition to ensure the uniqueness of scattered field

$$\lim_{\rho\to\infty}\rho^{\frac{1}{2}}(\partial_\rho\phi-\mathrm{i}\kappa_p\phi)=0, \quad \lim_{\rho\to\infty}\rho^{\frac{1}{2}}(\partial_\rho\psi-\mathrm{i}\kappa_s\psi)=0, \quad \rho=|\mathbf{x}|. \tag{2.8}$$

Once the potentials are found through the governing equation (2.6) and boundary conditions (2.7)-(2.8), the solutions of Navier equation can be calculated using the following relation

$$\boldsymbol{v}=[v_1 \;\; v_2]^{\mathrm{T}}=[\partial_x\phi+\partial_y\psi \;\; \partial_y\phi-\partial_x\psi]^{\mathrm{T}}. \tag{2.9}$$

From the wellposed of problem (2.2)-(2.4) and (2.6)-(2.8), we can obtain the uniqueness of the Helmholtz decomposition. The result is stated in the following Remark and the brief illustration is given in Appendix.

Remark 2.1. Let $\boldsymbol{v}$ be the scattered field corresponding to the solution of the boundary value problem (2.2)-(2.4). Then the scattered field $\boldsymbol{v}$ can be decomposed using the Helmholtz decomposition $\boldsymbol{v}=\nabla\phi+\mathbf{curl}\psi$, where $\phi=-\kappa_p^{-2}\nabla\cdot\boldsymbol{v}$, $\psi=\kappa_s^{-2}curl\boldsymbol{v}$ are the solutions of the coupled boundary value problem (2.6)-(2.8), and the Helmholtz decomposition is unique.

However, since the obstacle scattering problem is an open domain problem, we need to introduce some techniques to truncate the problem domain for numerical calculation. In this paper, the well-known PML technique and TBC technique are used and given in the following subsection.

2.1 The reduced problem with PML

The PML technique is introduced for the scattering problem in this subsection. Fig. 2 shows a scattering domain with a square PML, where the bounded domain is denoted by Ω^{PML} and its boundary is $\partial\Omega^{PML}=\Gamma_D\bigcup\Gamma_p$. The domain Ω^{PML} can be described by

$$\Omega^{PML}=\big\{(x,y)|x_{\min}-d_x<x<x_{\max}+d_x,\ y_{\min}-d_y<y<y_{\max}+d_y\big\}\backslash\overline{D}, \tag{2.10}$$

where d_k, $(k=x,y)$ is the thickness of PML layer in k direction. Let $s_k(k)=\sigma_0(k)+\mathrm{i}\sigma_k(k)$, $k=x,y$ be the model medium property of PML in the domain Ω^{PML}, and satisfies

$$\begin{cases}\sigma_0=1, & \sigma_k=0, \quad \text{for } \ x_{\min}<x<x_{\max} \ \text{ or } \ y_{\min}<y<y_{\max},\\ \sigma_0=1, & \sigma_k>0, \quad \text{otherwise},\end{cases} \tag{2.11}$$

where $\mathrm{i}=\sqrt{(-1)}$ is an imaginary unit.

The PML is defined by the complex coordinate stretching

$$\hat{x}=\int_0^x s_x(\tau)d\tau, \quad \hat{y}=\int_0^y s_y(\tau)d\tau. \tag{2.12}$$

The form of the governing equation satisfied by the potentials in the complex coordinate system $(\hat{x}, \hat{y})$ is the same as that of the original governing equation (2.6), which has been given in [44], i.e.,

$$\Delta_{\hat{\mathbf{x}}}\phi+\kappa_p^2\phi=0, \quad \Delta_{\hat{\mathbf{x}}}\psi+\kappa_s^2\psi=0 \quad \text{in } \ \Omega^{PML}, \tag{2.13}$$

where $\Delta_{\hat{\mathbf{x}}}=\partial^2_{\hat{x}\hat{x}}+\partial^2_{\hat{y}\hat{y}}$. According to Eq. (2.12) and chain rule, we have following relations

$$\frac{\partial}{\partial\hat{x}}=\frac{1}{s_x(x)}\frac{\partial}{\partial x}, \quad \frac{\partial}{\partial\hat{y}}=\frac{1}{s_y(y)}\frac{\partial}{\partial y}. \tag{2.14}$$

Based on the above transformation, the Eq. (2.13) becomes

$$\nabla\cdot(A\nabla\phi)+\kappa_p^2 s_x s_y\phi=0, \quad \nabla\cdot(A\nabla\psi)+\kappa_s^2 s_x s_y\psi=0 \quad \text{in } \ \Omega^{PML}, \tag{2.15}$$

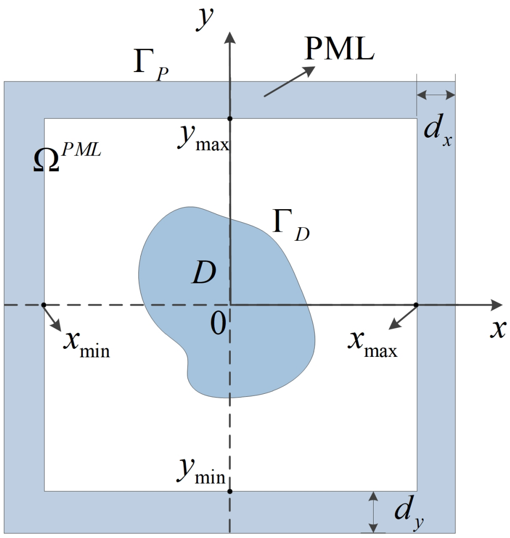

Figure 2: The problem geometry of obstacle scattering with PML.

where

$$A = \begin{bmatrix} s_y/s_x & 0 \\ 0 & s_x/s_y \end{bmatrix}$$

is the parameter matrix.

According to the wave decays exponentially in the PML [10], we apply the Dirichlet conditions on the outer boundary of PML

$$\phi=0, \quad \psi=0 \quad \text{on } \Gamma_p. \tag{2.16}$$

2.2 The reduced problem with TBC

The TBC technique is introduced for the scattering problem in this subsection. After imposing TBC on Γ_B, the truncated bounded domain is represented by Ω^{TBC} with the boundary $\partial\Omega^{TBC}=\Gamma_D \bigcup \Gamma_B$, as shown in Fig. 3. The transparent boundary Γ_B is a circle with the radius R.

As is known, the exterior Helmholtz equations (2.6) in Ω can be analytically solved with the following Fourier series forms

$$\phi(r,\theta)=\frac{1}{\pi}\sum_{n=0}^{\infty}{}' \int_0^{2\pi} \frac{H_n^{(1)}(\kappa_p r)}{H_n^{(1)}(\kappa_p R)} \cos n(\theta-\theta')\phi(R,\theta')d\theta', \tag{2.17a}$$

$$\psi(r,\theta)=\frac{1}{\pi}\sum_{n=0}^{\infty}{}' \int_0^{2\pi} \frac{H_n^{(1)}(\kappa_s r)}{H_n^{(1)}(\kappa_s R)} \cos n(\theta-\theta')\psi(R,\theta')d\theta', \tag{2.17b}$$

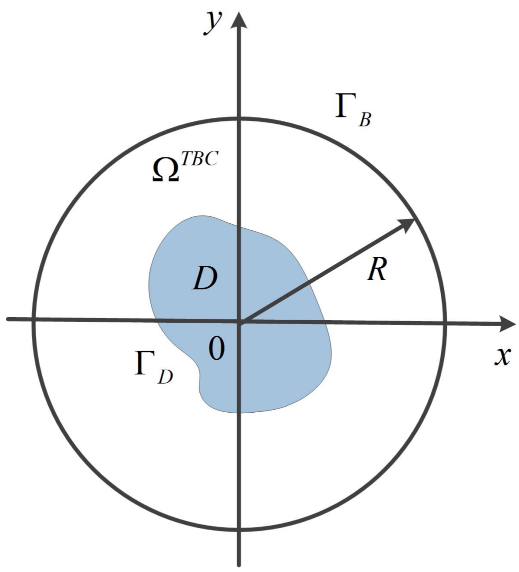

Figure 3: The problem geometry of obstacle scattering with TBC.

where $\phi(R,\theta')$ and $\psi(R,\theta')$ are prescribed Dirichlet data on Γ_B. $H_n^{(1)}$ is the Hankel function of the first kind with n order, and the prime after the sum indicates that the first term of the series needs to be multiplied by $\frac{1}{2}$.

Take the normal derivative of ϕ, ψ in Eq. (2.17), we have

$$\frac{\partial\phi(r,\theta)}{\partial \mathrm{n}}\Big|_{r=R} = -\sum_{n=0}^{\infty}{}' \int_0^{2\pi} m_1(\theta-\theta')\phi(R,\theta')d\theta' = -M_1\phi(R,\theta) \qquad \text{on } \Gamma_B, \tag{2.18a}$$

$$\frac{\partial\psi(r,\theta)}{\partial \mathrm{n}}\Big|_{r=R} = -\sum_{n=0}^{\infty}{}' \int_0^{2\pi} m_2(\theta-\theta')\psi(R,\theta')d\theta' = -M_2\psi(R,\theta) \qquad \text{on } \Gamma_B, \tag{2.18b}$$

where M_1, M_2 are the DtN operators, as called TBC [42], the coefficients $m_1(\theta-\theta')$, $m_2(\theta-\theta')$ are written as

$$m_1(\theta-\theta') = -\frac{\kappa_p}{\pi}\frac{H_n^{(1)'}(\kappa_p R)}{H_n^{(1)}(\kappa_p R)}(\cos n\theta \cos n\theta' + \sin n\theta \sin n\theta'), \tag{2.19a}$$

$$m_2(\theta-\theta') = -\frac{\kappa_s}{\pi}\frac{H_n^{(1)'}(\kappa_s R)}{H_n^{(1)}(\kappa_s R)}(\cos n\theta \cos n\theta' + \sin n\theta \sin n\theta'). \tag{2.19b}$$

3 Formulation of NS-FEM with the linear gradient field

This section firstly introduces the node-based SD (N-SD) and the weakened weak formulation of NS-FEM. Then the linear gradient field is constructed on each N-SD using polynomial basis with the complete first order for 2D and the unknown coefficients can be solved by three linear independent weight functions. Based on the linear gradient function, a modified smoothed gradient matrix can be calculated for each N-SD.

3.1 Node-based smoothing domains

In this subsection, k-th N-SD is constructed by successively connecting centroid of the element and midpoint of the edge adjacent to the k-th node. The number of N-SDs is the same as that of nodes. Fig. 4 with 19 N-SDs is constructed by 24 triangular element meshes.

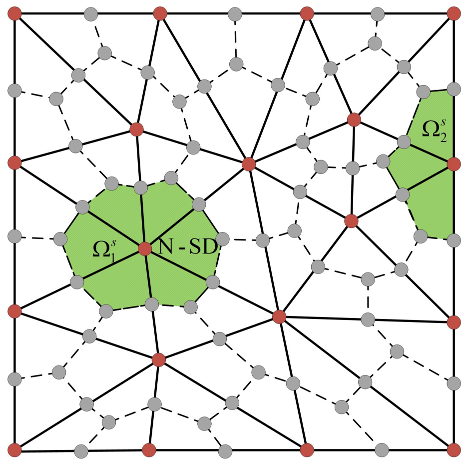

Figure 4: The original triangular elements (solid lines) and N-SD (dashed lines).

3.2 The gradient approximation for original NS-FEM

The gradient of a scalar function indicates the direction derivative of the function at one point, which is frequently used in the weak form of the standard FEM. The standard FEM is based on the linear Lagrange element in this paper. Assuming that the potentials can be approximated by interpolation of shape functions, we have

$$\phi(\mathbf{x})=\sum_{i=1}^{N_p}N_i(\mathbf{x})\overline{\phi}_i,\quad \psi(\mathbf{x})=\sum_{i=1}^{N_p}N_i(\mathbf{x})\overline{\psi}_i, \tag{3.1}$$

where N_p represents the number of nodes in the mesh, $\overline{\phi}_i$ and $\overline{\psi}_i$ are the values of potentials ϕ and ψ at the node $\mathbf{x}_i$, i.e., $\overline{\phi}_i=\phi(\mathbf{x}_i)$ and $\overline{\psi}_i=\psi(\mathbf{x}_i)$; $N_i(\mathbf{x})$ is the nodal shape function in the standard FEM and S-FEM.

In the standard FEM, the gradients of potentials need to be evaluated using the following relation

$$\nabla\phi=\mathbf{L}_d\phi=\sum_{i=1}^{N_p}\mathbf{L}_dN_i(\mathbf{x})\overline{\phi}_i=\sum_{i=1}^{N_p}\mathbf{B}_i\overline{\phi}_i, \tag{3.2a}$$

$$\nabla\psi=\mathbf{L}_d\psi=\sum_{i=1}^{N_p}\mathbf{L}_dN_i(\mathbf{x})\overline{\psi}_i=\sum_{i=1}^{N_p}\mathbf{B}_i\overline{\phi}_i, \tag{3.2b}$$

where $\mathbf{B}_i=\mathbf{L}_dN_i(\mathbf{x})=[\partial N_i/\partial x \;\; \partial N_i/\partial y]^{\mathrm{T}}$ is the gradient matrix, in which $\mathbf{L}_d=[\partial_x \;\; \partial_y]^{\mathrm{T}}$ is a 2D gradient operator. It is evident that the derivatives of shape functions are needed in this calculation.

In the original NS-FEM, using the generalized smoothing operation, the smoothed gradients of potentials are evaluated as follows

$$\nabla\phi=\sum_{k=1}^{N_s}\int_{\Omega_k^s}\mathbf{L}_d\phi(\mathbf{x})w(\mathbf{x}_k-\mathbf{x})d\Omega, \quad \nabla\psi=\sum_{k=1}^{N_s}\int_{\Omega_k^s}\mathbf{L}_d\psi(\mathbf{x})w(\mathbf{x}_k-\mathbf{x})d\Omega, \tag{3.3}$$

where N_s is the number of smoothing domains, $w(\mathbf{x}_k-\mathbf{x})$ is a weight function associated with $\mathbf{x}_k$, and Ω_k^s is the k-th N-SD. The weight function takes the Heaviside-type function and has the following

$$w(\mathbf{x}_k-\mathbf{x})=\begin{cases}\dfrac{1}{A_k^s}, & \mathbf{x}\in\Omega_k^s,\\ 0, & \mathbf{x}\notin\Omega_k^s,\end{cases} \tag{3.4}$$

where A_k^s is the area of smoothing domain.

Using the Green's divergence theorem and $\mathbf{L}_dw(\mathbf{x}_k-\mathbf{x})=\mathbf{0}$, the smoothed gradient given in Eq. (3.3) can be rewritten as

$$\nabla\phi=\sum_{k=1}^{N_s}\int_{\Omega_k^s}\mathbf{L}_d\phi(\mathbf{x})w(\mathbf{x}_k-\mathbf{x})d\Omega=\sum_{i=1}^{N_s}\frac{1}{A_k^s}\int_{\Gamma_k^s}\mathbf{L}_n\phi(\mathbf{x})d\Gamma, \tag{3.5a}$$

$$\nabla\psi=\sum_{k=1}^{N_s}\int_{\Omega_k^s}\mathbf{L}_d\psi(\mathbf{x})w(\mathbf{x}_k-\mathbf{x})d\Omega=\sum_{i=1}^{N_s}\frac{1}{A_k^s}\int_{\Gamma_k^s}\mathbf{L}_n\psi(\mathbf{x})d\Gamma, \tag{3.5b}$$

where $\mathbf{L}_n(\mathbf{x})=[n_x \;\; n_y]^{\mathbf{T}}$ is the unit outward normal vector. From Eq. (3.5), we find that the smoothed gradients are constants inside each smoothing domain, and can be written as

$$\nabla\phi=\sum_{i=1}^{N_s}\frac{1}{A_k^s}\int_{\Gamma_k^s}\mathbf{L}_nN_k(\mathbf{x})d\Gamma\overline{\phi}_k=\sum_{k=1}^{N_s}\hat{\mathbf{B}}_k(\mathbf{x})\overline{\phi}_k, \tag{3.6a}$$

$$\nabla\psi=\sum_{i=1}^{N_s}\frac{1}{A_k^s}\int_{\Gamma_k^s}\mathbf{L}_nN_k(\mathbf{x})d\Gamma\overline{\psi}_k=\sum_{k=1}^{N_s}\hat{\mathbf{B}}_k(\mathbf{x})\overline{\psi}_k, \tag{3.6b}$$

where $\hat{\mathbf{B}}(\mathbf{x})=[b_{kx}\ \ b_{ky}]^{\mathrm{T}}$, and b_{kl} is evaluated using the following Gauss quadrature

$$b_{kl}=\frac{1}{A_k^s}\int_{\Gamma_k^s} n_l(\mathbf{x})N_k(\mathbf{x})d\Gamma=\frac{1}{A_k^s}\sum_{q=1}^{N_k^{seg}}\Big(\sum_{g=1}^{N_g} w_g n_l(\mathbf{x}_g)N_k(\mathbf{x}_g)L_q\Big),\quad l=x,y, \tag{3.7}$$

where N_k^{seg} is the number of segments on the boundary Γ_k^s; L_q is the length of the q-th segment in the k-th smoothing domain. N_g is the number of the Gauss points $\mathbf{x}_g$ in each segment and w_g is the Gauss weight coefficient. Generally, one Gauss-point is used for 2D problem.

3.3 The construction of linear gradient field

The N-SDs are constructed by adjacent parts of the nodes in the finite element mesh, and the smoothed gradients are constants (simply averaging) in each smoothing domain. Hence the constant gradient is a rough approximation and cannot reflect gradient changes over the smoothing domain Ω_k^s for the real gradient, which may lose accuracy.

To cure this defect of original NS-FEM, the changes of gradients of potentials should be considered. Recently, Li and Liu [41] reconstructed the smoothed derivatives of functions by using the pick-out technique and high-order smoothed strain field for mechanics problems, which can overcome the overly-soft deficiency of NS-FEM.

Assuming that the gradient functions are linearly continuous variation with respect to x and y in smoothing domain Ω_k^s, and have the following Taylor expansion form at point $\mathbf{x}=(x_k,y_k)$,

$$\overline{\nabla W}(\mathbf{x})=c_0+c_x(x-x_k)+c_y(y-y_k),\quad W=\phi,\psi, \tag{3.8}$$

where $c_0=[c_{01}\ \ c_{02}]^{\mathrm{T}}$, $c_x=[c_{x1}\ \ c_{x2}]^{\mathrm{T}}$, $c_y=[c_{y1}\ \ c_{y2}]^{\mathrm{T}}$, are unknown coefficients. According to the S-FEM theory, when the weight function is continuous, the gradient function and the smoothed gradient function are equal in the integral sense, i.e.,

$$\int_{\Omega_k^s}\nabla W(\mathbf{x})w(\mathbf{x}-\mathbf{x}_k)d\Omega=\int_{\Omega_k^s}\overline{\nabla W}(\mathbf{x})w(\mathbf{x}-\mathbf{x}_k)d\Omega, \tag{3.9}$$

where $w(\mathbf{x}-\mathbf{x}_k)$ is a continuous weight function in Ω_k^s. Substituting Eq. (3.8) into Eq. (3.9), we have

$$\int_{\Omega_k^s}\nabla W(\mathbf{x})w(\mathbf{x}-\mathbf{x}_k)d\Omega=\int_{\Omega_k^s}(c_0+c_x(x-x_k)+c_y(y-y_k))w(\mathbf{x}-\mathbf{x}_k)d\Omega. \tag{3.10}$$

In order to determine coefficients c_0, c_x, c_y, three linearly independent weight functions are established about the node $\mathbf{x}_k$ in the smoothing domain Ω_k^s as

$$w_1(\mathbf{x}-\mathbf{x}_k)=\frac{1}{M_0},\quad w_2(\mathbf{x}-\mathbf{x}_k)=\frac{x-x_k}{M_{xx}},\quad w_3(\mathbf{x}-\mathbf{x}_k)=\frac{y-y_k}{M_{yy}}. \tag{3.11}$$

Substituting three weight functions given in Eq. (3.11) into Eq. (3.10), we have

$$\frac{1}{M_0}\int_{\Omega_k^s}\nabla W(\mathbf{x})d\Omega = c_0 + c_x\frac{M_x}{M_0} + c_y\frac{M_y}{M_0}, \tag{3.12a}$$

$$\frac{1}{M_{xx}}\int_{\Omega_k^s}\nabla W(\mathbf{x})(x-x_k)d\Omega = c_0\frac{M_x}{M_{xx}} + c_x + c_y\frac{M_{xy}}{M_{xx}}, \tag{3.12b}$$

$$\frac{1}{M_{yy}}\int_{\Omega_k^s}\nabla W(\mathbf{x})(y-y_k)d\Omega = c_0\frac{M_y}{M_{yy}} + c_x\frac{M_{xy}}{M_{yy}} + c_y, \tag{3.12c}$$

where M_0 is the zeroth moment; M_x and M_y are the first moments; M_{xx}, M_{xy} and M_{yy} are the second moments. They can be expressed as

$$M_0 = A_k^s, \qquad M_x = \int_{\Omega_k^s}(x-x_k)d\Omega, \qquad M_y = \int_{\Omega_k^s}(y-y_k)d\Omega, \tag{3.13a}$$

$$M_{xx} = \int_{\Omega_k^s}(x-x_k)^2 d\Omega, \quad M_{xy} = \int_{\Omega_k^s}(x-x_k)(y-y_k)d\Omega, \quad M_{yy} = \int_{\Omega_k^s}(y-y_k)^2 d\Omega. \tag{3.13b}$$

Note that these moments can be calculated by formulas provided by Liggestt [43]. The left terms of Eqs. (3.12a)-(3.12c) form a vector, which is noted as

$$\mathbf{g} = \left[\frac{1}{M_0}\int_{\Omega_k^s}\nabla W(\mathbf{x})d\Omega \quad \frac{1}{M_{xx}}\int_{\Omega_k^s}\nabla W(\mathbf{x})(x-x_k)d\Omega \quad \frac{1}{M_{yy}}\int_{\Omega_k^s}\nabla W(\mathbf{x})(y-y_k)d\Omega\right]^{\mathrm{T}},$$

and can also be rewritten as

$$\begin{bmatrix} g_{01} & g_{02} & g_{x1} & g_{x2} & g_{y1} & g_{y2}\end{bmatrix}^{\mathrm{T}},$$

where

$$\begin{aligned}
g_{01} &= \frac{1}{M_0}\int_{\Omega_k^s}\partial_x W(\mathbf{x})d\Omega, & g_{02} &= \frac{1}{M_0}\int_{\Omega_k^s}\partial_y W(\mathbf{x})d\Omega,\\
g_{x1} &= \frac{1}{M_{xx}}\int_{\Omega_k^s}\partial_x W(\mathbf{x})(x-x_k)d\Omega, & g_{x2} &= \frac{1}{M_{xx}}\int_{\Omega_k^s}\partial_y W(\mathbf{x})(x-x_k)d\Omega,\\
g_{y1} &= \frac{1}{M_{yy}}\int_{\Omega_k^s}\partial_x W(\mathbf{x})(y-y_k)d\Omega, & g_{y2} &= \frac{1}{M_{yy}}\int_{\Omega_k^s}\partial_y W(\mathbf{x})(y-y_k)d\Omega.
\end{aligned}$$

Then Eqs. (3.12a)-(3.12c) can be rewritten into the following matrix form

$$\mathbf{M}\mathbf{c}_1 = \mathbf{g}_1, \quad \mathbf{M}\mathbf{c}_2 = \mathbf{g}_2, \tag{3.14}$$

where

$$\mathbf{M} = \begin{bmatrix} 1 & M_x/M_0 & M_y/M_0 \\ M_x/M_{xx} & 1 & M_{xy}/M_{xx} \\ M_y/M_{yy} & M_{xy}/M_{yy} & 1\end{bmatrix},$$

$$\mathbf{c}_1 = \begin{bmatrix} c_{01} & c_{x1} & c_{y1}\end{bmatrix}^{\mathrm{T}}, \qquad \mathbf{c}_2 = \begin{bmatrix} c_{02} & c_{x2} & c_{y2}\end{bmatrix}^{\mathrm{T}},$$

$$\mathbf{g}_1 = \begin{bmatrix} g_{01} & g_{x1} & g_{y1}\end{bmatrix}^{\mathrm{T}}, \qquad \mathbf{g}_2 = \begin{bmatrix} g_{02} & g_{x2} & g_{y2}\end{bmatrix}^{\mathrm{T}}.$$

Since the nominal orders of the three smoothing functions are different, the matrix is linearly independent and invertible, which can be denoted by

$$\mathbf{M}^{-1}=\begin{bmatrix} m'_{11} & m'_{12} & m'_{13} \\ m'_{21} & m'_{22} & m'_{23} \\ m'_{31} & m'_{32} & m'_{33} \end{bmatrix}. \tag{3.15}$$

Then the unknowns can be solved by

$$\mathbf{c}_1=\mathbf{M}^{-1}\mathbf{g}_1, \quad \mathbf{c}_2=\mathbf{M}^{-1}\mathbf{g}_2, \tag{3.16}$$

where $\mathbf{g}_1$, $\mathbf{g}_2$ can be evaluated by applying Green's theorem to $\mathbf{g}$, and we get

$$\mathbf{g}=\begin{bmatrix} \dfrac{1}{M_0}\displaystyle\int_{\Gamma_k^s}\mathbf{L}_n W(\mathbf{x})d\Gamma \\ \dfrac{1}{M_{xx}}\left[\displaystyle\int_{\Gamma_k^s}\mathbf{L}_n W(\mathbf{x})(x-x_k)d\Gamma-\int_{\Omega_k^s}\mathbf{L}_d(x-x_k)W(\mathbf{x})d\Omega\right] \\ \dfrac{1}{M_{yy}}\left[\displaystyle\int_{\Gamma_k^s}\mathbf{L}_n W(\mathbf{x})(y-y_k)d\Gamma-\int_{\Omega_k^s}\mathbf{L}_d(y-y_k)W(\mathbf{x})d\Omega\right] \end{bmatrix}. \tag{3.17}$$

The potentials can be approximated by interpolation of shape functions

$$\mathbf{W}(\mathbf{x})=\begin{bmatrix} N_1 & N_2 & \cdots & N_{N_p} \end{bmatrix}\begin{bmatrix} W_1 & W_2 & \cdots & W_{N_p} \end{bmatrix}^{\mathrm{T}}=\mathbf{N}^{\mathrm{T}}\mathbf{W}, \quad W=\phi,\psi. \tag{3.18}$$

Substituting the above equation into Eq. (3.17), we have

$$\mathbf{g}=\begin{bmatrix} \dfrac{1}{M_0}\displaystyle\int_{\Gamma_k^s}\mathbf{L}_n\mathbf{N}(\mathbf{x})^{\mathrm{T}}d\Gamma\mathbf{W} \\ \dfrac{1}{M_{xx}}\left[\displaystyle\int_{\Gamma_k^s}\mathbf{L}_n\mathbf{N}(\mathbf{x})(x-x_k)d\Gamma-\int_{\Omega_k^s}\mathbf{L}_d(x-x_k)\mathbf{N}(\mathbf{x})^{\mathrm{T}}d\Omega\right]\mathbf{W} \\ \dfrac{1}{M_{yy}}\left[\displaystyle\int_{\Gamma_k^s}\mathbf{L}_n\mathbf{N}(\mathbf{x})(y-y_k)d\Gamma-\int_{\Omega_k^s}\mathbf{L}_d(y-y_k)\mathbf{N}(\mathbf{x})^{\mathrm{T}}d\Omega\right]\mathbf{W} \end{bmatrix}=\begin{bmatrix} \mathbf{B}_0^c\mathbf{W} \\ \mathbf{B}_x^c\mathbf{W} \\ \mathbf{B}_y^c\mathbf{W} \end{bmatrix}. \tag{3.19}$$

Therefore, using Eqs. (3.8), (3.15), (3.16) and (3.19), the smoothed gradient can be expressed as

$$\overline{\nabla W}(\mathbf{x})=[\bar{\mathbf{B}}_{k0}^s+\bar{\mathbf{B}}_{kx}^s(x-x_k)+\bar{\mathbf{B}}_{ky}^s(y-y_k)]\mathbf{W}=\bar{\mathbf{B}}(\mathbf{x})\mathbf{W}, \tag{3.20}$$

where $\bar{\mathbf{B}}(\mathbf{x})$ is the modified smoothed gradient matrix, and $\bar{\mathbf{B}}_{k0}^s$, $\bar{\mathbf{B}}_{kx}^s$, $\bar{\mathbf{B}}_{ky}^s$ are calculated as follows

$$\begin{cases} \bar{\mathbf{B}}_{k0}^s=m'_{11}\mathbf{B}_0^c+m'_{12}\mathbf{B}_x^c+m'_{13}\mathbf{B}_y^c, \\ \bar{\mathbf{B}}_{kx}^s=m'_{21}\mathbf{B}_0^c+m'_{22}\mathbf{B}_x^c+m'_{23}\mathbf{B}_y^c, \\ \bar{\mathbf{B}}_{ky}^s=m'_{31}\mathbf{B}_0^c+m'_{32}\mathbf{B}_x^c+m'_{33}\mathbf{B}_y^c. \end{cases}$$

4 The discretized formulation for NS-FEM-L

In this subsection, we discuss the approximation formulations of coupled boundary problem by using NS-FEM-L model. Two truncated techniques (PML and TBC) are used in the discretized formulations and are named as NS-FEM-L-PML and NS-FEM-L-TBC, respectively. Based on this weak form in FEM and the linear smoothed gradient in Subsection 3.3, the weakened weak formulations of two NS-FEM-L models are given as follows for elastic wave obstacle scattering problem.

4.1 NS-FEM-L with PML

The NS-FEM-L formulations with PML are considered in this subsection. By using the second scalar Green's theorem, the weak forms of Eq. (2.15), Eq. (2.7) and Eq. (2.16) are as follows

$$\begin{cases} \int_{\Omega^{PML}} (A\nabla\phi)\cdot\nabla\xi d\Omega - \kappa_p^2 \int_{\Omega^{PML}} s_x s_y \phi\xi d\Omega + \int_{\Gamma_D} \partial_\tau \psi \xi d\Gamma = \int_{\Gamma_D} f\xi d\Gamma, \\ \int_{\Omega^{PML}} (A\nabla\psi)\cdot\nabla\eta d\Omega - \kappa_s^2 \int_{\Omega^{PML}} s_x s_y \psi\eta d\Omega + \int_{\Gamma_D} \partial_\tau \phi \eta d\Gamma = \int_{\Gamma_D} g\eta d\Gamma, \end{cases} \tag{4.1}$$

where ξ and η are test functions. The weakened weak forms of Eq. (4.1) by using the smoothing operator can be written as

$$\begin{cases} \sum_{k=1}^{N_s} \int_{\Omega_k^s} (\overline{\nabla\xi})\cdot(A\overline{\nabla\phi}) d\Omega - \kappa_p^2 \int_{\Omega^{PML}} s_x s_y \xi\phi d\Omega + \int_{\Gamma_D} \xi \partial_\tau \psi d\Gamma = \int_{\Gamma_D} \xi f d\Gamma, \\ \sum_{k=1}^{N_s} \int_{\Omega_k^s} (\overline{\nabla\eta})\cdot(A\overline{\nabla\psi}) d\Omega - \kappa_s^2 \int_{\Omega^{PML}} s_x s_y \eta\psi d\Omega + \int_{\Gamma_D} \eta \partial_\tau \phi d\Gamma = \int_{\Gamma_D} \eta g d\Gamma. \end{cases} \tag{4.2}$$

According to Eq. (3.20), the above equations can be written as the following matrix form

$$[\overline{\mathbf{K}} - \mathbf{P} + \mathbf{K}_b]\mathbf{\Phi} = \mathbf{F}, \tag{4.3}$$

where $\mathbf{\Phi} = [\boldsymbol{\phi} \ \ \boldsymbol{\psi}]^{\mathrm{T}}$ denotes an unknown nodal vector, in which $\boldsymbol{\phi}$ and $\boldsymbol{\psi}$ consist of $\boldsymbol{\phi}^e$ and $\boldsymbol{\psi}^e$, respectively. The modified smoothed stiffness matrix $\overline{\mathbf{K}}$ possesses a "close-to-exact" stiffness and can be formed as follows

$$\overline{\mathbf{K}} = \begin{bmatrix} \overline{\mathbf{K}}_1 & 0 \\ 0 & \overline{\mathbf{K}}_2 \end{bmatrix}, \tag{4.4}$$

in which

$$\overline{\mathbf{K}}_1 = \overline{\mathbf{K}}_2 = \sum_{k=1}^{N_n} \left(\overline{\mathbf{K}}_{k0}^s + \overline{\mathbf{K}}_{kx}^s + \overline{\mathbf{K}}_{ky}^s + \overline{\mathbf{K}}_{kxx}^s + \overline{\mathbf{K}}_{kxy}^s + \overline{\mathbf{K}}_{kyy}^s \right),$$

and can be expressed as

$$\overline{\mathbf{K}}_{k0}^{s}=A_{k}^{s}(\bar{\mathbf{B}}_{k0}^{s})^{\mathrm{T}}A\bar{\mathbf{B}}_{k0}^{s},\qquad \overline{\mathbf{K}}_{kx}^{s}=\Big((\bar{\mathbf{B}}_{k0}^{s})^{\mathrm{T}}A\bar{\mathbf{B}}_{kx}^{s}+(\bar{\mathbf{B}}_{kx}^{s})^{\mathrm{T}}A\bar{\mathbf{B}}_{k0}^{s}\Big)M_{x},\tag{4.5a}$$

$$\overline{\mathbf{K}}_{ky}^{s}=\Big((\bar{\mathbf{B}}_{k0}^{s})^{\mathrm{T}}A\bar{\mathbf{B}}_{ky}^{s}+\bar{\mathbf{B}}_{ky}^{s})^{\mathrm{T}}A\bar{\mathbf{B}}_{k0}^{s}\Big)M_{y},\qquad \overline{\mathbf{K}}_{kxx}^{s}=\big(\bar{\mathbf{B}}_{kx}^{s}\big)^{\mathrm{T}}A\bar{\mathbf{B}}_{kx}^{s}M_{xx},\tag{4.5b}$$

$$\overline{\mathbf{K}}_{kxy}^{s}=\Big((\bar{\mathbf{B}}_{kx}^{s})^{\mathrm{T}}A\bar{\mathbf{B}}_{ky}^{s}+(\bar{\mathbf{B}}_{ky}^{s})^{\mathrm{T}}A\bar{\mathbf{B}}_{kx}^{s}\Big)M_{xy},\quad \overline{\mathbf{K}}_{kyy}^{s}=\Big(\bar{\mathbf{B}}_{ky}^{s}\Big)^{\mathrm{T}}A\bar{\mathbf{B}}_{ky}^{s}M_{yy}.\tag{4.5c}$$

The mass matrix $\mathbf{P}$ consists of element mass matrix $\mathbf{P}^{e}$, and

$$\mathbf{P}^{e}=\begin{bmatrix}\kappa_{p}^{2}\mathbf{P}_{1}^{e} & 0\\ 0 & \kappa_{s}^{2}\mathbf{P}_{2}^{e}\end{bmatrix},\quad \mathbf{P}_{1}^{e}=\mathbf{P}_{2}^{e}=\int_{\Omega_{e}^{PML}}s_{x}s_{y}\mathbf{N}^{\mathrm{T}}\mathbf{N}d\Omega.\tag{4.6}$$

The boundary stiffness matrix is

$$\mathbf{K}_{b}^{e}=\begin{bmatrix}0 & \kappa_{p}^{2}\mathbf{b}_{1}^{e}\\ -\kappa_{s}^{2}\mathbf{b}_{2}^{e} & 0\end{bmatrix},\qquad \mathbf{b}_{1}^{e}=\mathbf{b}_{2}^{e}=\int_{\Gamma_{e}^{D}}\mathbf{N}^{\mathrm{T}}\boldsymbol{\tau}^{\mathrm{T}}\mathbf{N}d\Gamma.\tag{4.7}$$

The boundary element force vector $\mathbf{K}_{b}^{e}$ is

$$\mathbf{F}^{e}=\begin{bmatrix}\mathbf{F}_{1}^{e} & \mathbf{F}_{2}^{e}\end{bmatrix}^{\mathrm{T}},\quad \mathbf{F}_{1}^{e}=\int_{\Gamma_{e}^{D}}\mathbf{N}^{\mathrm{T}}fd\Gamma,\quad \mathbf{F}_{2}^{e}=\int_{\Gamma_{e}^{D}}\mathbf{N}^{\mathrm{T}}gd\Gamma.\tag{4.8}$$

4.2 NS-FEM-L with TBC

The NS-FEM-L formulations with TBC of the coupled boundary problem are discussed in this subsection. Based on the second scalar Green's theorem, we have the following weak forms of Eqs. (2.6), (2.7) and (2.18)

$$\begin{cases}\displaystyle\int_{\Omega^{TBC}}(\nabla\phi)\cdot\nabla\xi d\Omega-\kappa_{p}^{2}\int_{\Omega^{TBC}}\phi\xi d\Omega+\int_{\Gamma_{B}}M_{1}\phi\xi d\Gamma+\int_{\Gamma_{D}}\partial_{\tau}\psi\xi d\Gamma=\int_{\Gamma_{D}}f\xi d\Gamma,\\ \displaystyle\int_{\Omega^{TBC}}(\nabla\psi)\cdot\nabla\eta d\Omega-\kappa_{s}^{2}\int_{\Omega^{TBC}}\psi\eta d\Omega+\int_{\Gamma_{B}}M_{2}\psi\eta d\Gamma+\int_{\Gamma_{D}}\partial_{\tau}\phi\eta d\Gamma=\int_{\Gamma_{D}}g\eta d\Gamma,\end{cases}\tag{4.9}$$

where ξ and η are test functions. By using the smoothing operator, the weakened weak forms of the above equations are written as

$$\begin{cases}\displaystyle\sum_{k=1}^{N_{s}}\int_{\Omega_{k}^{s}}(\overline{\nabla\xi})^{\mathrm{T}}\cdot\overline{\nabla\phi}d\Omega-\kappa_{p}^{2}\int_{\Omega^{TBC}}\xi\phi d\Omega+\int_{\Gamma_{B}}\xi M_{1}\phi d\Gamma+\int_{\Gamma_{D}}\xi\partial_{\tau}\psi d\Gamma=\int_{\Gamma_{D}}\xi fd\Gamma,\\ \displaystyle\sum_{k=1}^{N_{s}}\int_{\Omega_{k}^{s}}(\overline{\nabla\eta})^{\mathrm{T}}\cdot\overline{\nabla\psi}d\Omega-\kappa_{s}^{2}\int_{\Omega^{TBC}}\eta\psi d\Omega+\int_{\Gamma_{B}}\eta M_{2}\psi d\Gamma+\int_{\Gamma_{D}}\eta\partial_{\tau}\phi d\Gamma=\int_{\Gamma_{D}}\eta gd\Gamma.\end{cases}\tag{4.10}$$

According to the modified smoothed gradients given in Eq. (3.20), we have the matrix form

$$[\overline{\mathbf{K}}-\mathbf{P}-\mathbf{T}-\mathbf{K}_{b}]\boldsymbol{\Phi}=\mathbf{F},\tag{4.11}$$

where $\mathbf{\Phi}=[\boldsymbol{\phi}\ \ \boldsymbol{\psi}]^{\mathrm{T}}$ denotes an unknown nodal vector. Note that the obstacle boundary stiffness matrix $\mathbf{K}_b$ and the vector $\mathbf{F}$ can be calculated as in Subsection 4.1. The system stiffness matrix using the linear smoothed gradients can be calculated by

$$\overline{\mathbf{K}}=\begin{bmatrix}\overline{\mathbf{K}}_1 & 0\\ 0 & \overline{\mathbf{K}}_2\end{bmatrix}, \tag{4.12}$$

where

$$\overline{\mathbf{K}}_1=\overline{\mathbf{K}}_2=\sum_{k=1}^{N_n}(\overline{\mathbf{K}}_{k0}^s+\overline{\mathbf{K}}_{kx}^s+\overline{\mathbf{K}}_{ky}^s+\overline{\mathbf{K}}_{kxx}^s+\overline{\mathbf{K}}_{kxy}^s+\overline{\mathbf{K}}_{kyy}^s),$$

and

$$\begin{aligned}
&\overline{\mathbf{K}}_{k0}^s=A_k^s(\bar{\mathbf{B}}_{k0}^s)^{\mathrm{T}}\bar{\mathbf{B}}_{k0}^s, &&\overline{\mathbf{K}}_{kx}^s=\Big((\bar{\mathbf{B}}_{k0}^s)^{\mathrm{T}}\bar{\mathbf{B}}_{kx}^s+(\bar{\mathbf{B}}_{kx}^s)^{\mathrm{T}}\bar{\mathbf{B}}_{k0}^s\Big)M_x,\\
&\overline{\mathbf{K}}_{ky}^s=\Big((\bar{\mathbf{B}}_{k0}^s)^{\mathrm{T}}\bar{\mathbf{B}}_{ky}^s+\bar{\mathbf{B}}_{ky}^s)^{\mathrm{T}}\bar{\mathbf{B}}_{k0}^s\Big)M_y, &&\overline{\mathbf{K}}_{kxx}^s=\big(\bar{\mathbf{B}}_{kx}^s\big)^{\mathrm{T}}\bar{\mathbf{B}}_{kx}^sM_{xx},\\
&\overline{\mathbf{K}}_{kxy}^s=\Big((\bar{\mathbf{B}}_{kx}^s)^{\mathrm{T}}\bar{\mathbf{B}}_{ky}^s+(\bar{\mathbf{B}}_{ky}^s)^{\mathrm{T}}\bar{\mathbf{B}}_{kx}^s\Big)M_{xy}, &&\overline{\mathbf{K}}_{kyy}^s=\Big(\bar{\mathbf{B}}_{ky}^s\Big)^{\mathrm{T}}\bar{\mathbf{B}}_{ky}^sM_{yy}.
\end{aligned}$$

The mass matrix $\mathbf{P}$ consists of the element mass matrix $\mathbf{P}^e$, and

$$\mathbf{P}^e=\begin{bmatrix}\kappa_p^2\mathbf{P}_1^e & 0\\ 0 & \kappa_s^2\mathbf{P}_2^e\end{bmatrix}, \tag{4.13}$$

where

$$\mathbf{P}_1^e=\mathbf{P}_2^e=\int_{\Omega_e^{TBC}}\mathbf{N}^{\mathrm{T}}\mathbf{N}d\Omega.$$

The matrix $\mathbf{T}$ is associated with the TBC and can be given by

$$\mathbf{T}=\begin{bmatrix}\mathbf{T}^1 & 0\\ 0 & \mathbf{T}^2\end{bmatrix}, \tag{4.14}$$

in which the element $\mathbf{T}_{ij}^l$ of matrix $\mathbf{T}^l$, $l=1,2$ at the i-th row and j-th column can be evaluated by

$$\begin{aligned}
\mathbf{T}_{ij}^1&=\int_{\Gamma_B}N_IM_1N_Jd\Gamma\\
&=-\sum_{j=0}^{\infty}\frac{\kappa_p}{\pi}\frac{H_n^{(1)'}(\kappa_pR)}{H_n^{(1)}(\kappa_pR)}\left(\int_{\Gamma_B}N_I(\mathbf{x})G(\theta)d\Gamma\right)\left(\int_{\Gamma_B}N_I(\mathbf{x})G(\theta')^{\mathrm{T}}d\Gamma\right), \qquad (4.15\mathrm{a})\\
\mathbf{T}_{ij}^2&=\int_{\Gamma_B}N_IM_2N_Jd\Gamma\\
&=-\sum_{j=0}^{\infty}\frac{\kappa_s}{\pi}\frac{H_n^{(1)'}(\kappa_sR)}{H_n^{(1)}(\kappa_sR)}\left(\int_{\Gamma_B}N_I(\mathbf{x})G(\theta)d\Gamma\right)\left(\int_{\Gamma_B}N_I(\mathbf{x})G(\theta')^{\mathrm{T}}d\Gamma\right), \qquad (4.15\mathrm{b})
\end{aligned}$$

where N_I and N_J are the shape functions related to node i and j, respectively. The function $G(\theta)$ is

$$G(\theta)=\begin{bmatrix}\cos n\theta & \sin n\theta\end{bmatrix}. \tag{4.16}$$

Once the potentials are found through the governing equation (2.6) and boundary conditions (2.7)-(2.8), the solutions of Navier equation can be calculated using Eq. (2.9).

5 Numerical experiments

In this section, the effectiveness of NS-FEM-L-PML and NS-FEM-LTBC models is studied through three numerical examples: the obstacle scattering with circle-shaped, ellipse-shaped and acorn-shaped, and compared with standard FEM model. The relative errors, L^2 error and H^1 semi-norm error are used to assess numerical solutions, which is performed through the analytic solutions for circle-shaped obstacle and the reference solutions for ellipse-shaped and acorn-shaped obstacles. The relative error (E_r), L^2 error (E_{L^2}) and H^1 semi-norm error (E_{H^1}) in the numerical computational domain Ω^N can be defined as follows

$$\mathrm{E}_r=\sqrt{\sum_{i=1}^{N}(\bar{\boldsymbol{v}}_i^e-\bar{\boldsymbol{v}}_i^n)^{\mathrm{T}}(\boldsymbol{v}_i^e-\boldsymbol{v}_i^n)\Big/\sum_{i=1}^{N}(\bar{\boldsymbol{v}}_i^e)(\boldsymbol{v}_i^e)}, \tag{5.1a}$$

$$\mathrm{E}_{L^2}=\sqrt{\int_{\Omega^N}(\bar{\boldsymbol{v}}^e-\bar{\boldsymbol{v}}^n)^{\mathrm{T}}(\boldsymbol{v}^e-\boldsymbol{v}^n)d\mathbf{x}}, \tag{5.1b}$$

$$\mathrm{E}_{H^1}=\sqrt{\int_{\Omega^N}(\nabla\bar{\boldsymbol{v}}^e-\nabla\bar{\boldsymbol{v}}^n)^{\mathrm{T}}(\nabla\boldsymbol{v}^e-\nabla\boldsymbol{v}^n)d\mathbf{x}}, \tag{5.1c}$$

where $\boldsymbol{v}$ denotes the solution of the problem, such as ϕ, ψ, or $[\phi\ \ \psi]$, and the supscript e and n denote the analytical/ reference solutions and the numerical solution, respectively. The subscript i denotes the value of the i-th node, $i=1,2,\cdots,N$, in which N is the number of nodes in the mesh. Besides, $\bar{\boldsymbol{v}}^e$ and $\bar{\boldsymbol{v}}^n$ are the corresponding complex conjugates.

5.1 Scattering by a cylinder with a circle cross section

We consider the scattering of a plane wave by a cylinder with a circle cross section, and the radius of the circle is R, as shown in Fig. 5. Assuming that the cylinder has no change in the z-axis direction, the problem is transformed into a two-dimensional problem.

The analytical solutions [5] with Fourier series expansions of this above problem in the polar coordinates are

$$\phi(r,\theta)=\sum_{n\in\mathbb{Z}}\frac{H_n^{(1)}(\kappa_p r)}{H_n^{(1)}(\kappa_p R)}\phi^{(n)}(R)e^{in\theta},\quad \psi(r,\theta)=\sum_{n\in\mathbb{Z}}\frac{H_n^{(1)}(\kappa_s r)}{H_n^{(1)}(\kappa_s R)}\psi^{(n)}(R)e^{in\theta}, \tag{5.2}$$

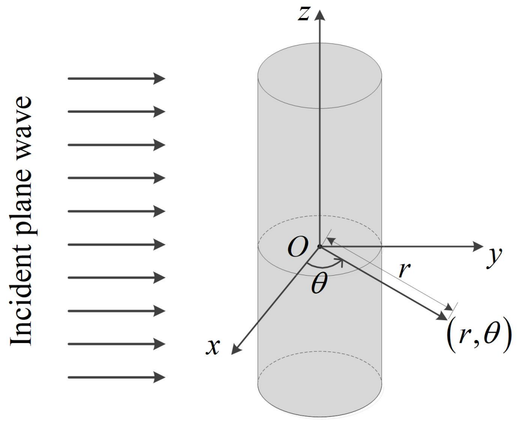

Figure 5: The geometry structure of scattering by a cylinder with a circle cross section.

where $\phi^{(n)}$ and $\psi^{(n)}$ are the Fourier modes of ϕ and ψ, and can be written as, respectively

$$\phi^{(n)}=c^{(n)}\left(\frac{\kappa_s H_n^{(1)'}(\kappa_s R)}{H_n^{(1)}(\kappa_s R)}f^{(n)}-\frac{\mathrm{i}n}{R}g^{(n)}\right), \tag{5.3a}$$

$$\psi^{(n)}=c^{(n)}\left(\frac{\mathrm{i}n}{R}f^{(n)}+\frac{\kappa_p H_n^{(1)'}(\kappa_p R)}{H_n^{(1)}(\kappa_p R)}g^{(n)}\right), \tag{5.3b}$$

in which

$$c^{(n)}=\frac{R^2H_n^{(1)}(\kappa_pR)H_n^{(1)}(\kappa_sR)}{R^2\kappa_p\kappa_sH_n^{(1)'}(\kappa_pR)H_n^{(1)'}(\kappa_sR)-n^2H_n^{(1)}(\kappa_pR)H_n^{(1)}(\kappa_sR)},$$

$f^{(n)}$ and $g^{(n)}$ are the Fourier modes of the periodic functions f and g with 2π period, and can be calculated by the fast Fourier transform (FFT).

In the calculation, only a single compressional wave is used to illuminate the obstacle, i.e., $\boldsymbol{u}^{inc}=\mathbf{d}e^{\mathrm{i}\kappa_p\mathbf{x}\cdot\mathbf{d}}$, which $\mathbf{d}=(1,0)$ is the propagation direction of wave. These parameters of obstacle, PML and TBC are listed in Table 1. The truncated domains with PML and TBC are shown in Fig. 6. In this example, the problem domains are discretized using the meshes with different sizes of triangular elements, which are generated using Matlab software.

The results of solving above scattering problem by using the NS-FEM with PML (NS-FEM-PML) and TBC (NS-FEM-TBC) techniques are shown in Fig. 7. It can be found that the numerical solutions of two NS-FEM models are much different from the exact solution and they are not extremely stable. The reason is that the NS-FEM model cause "over-soft" stiffness in the scattering problem. Therefore, this paper focuses on comparing the NS-FEM-L and FEM models from different aspects.

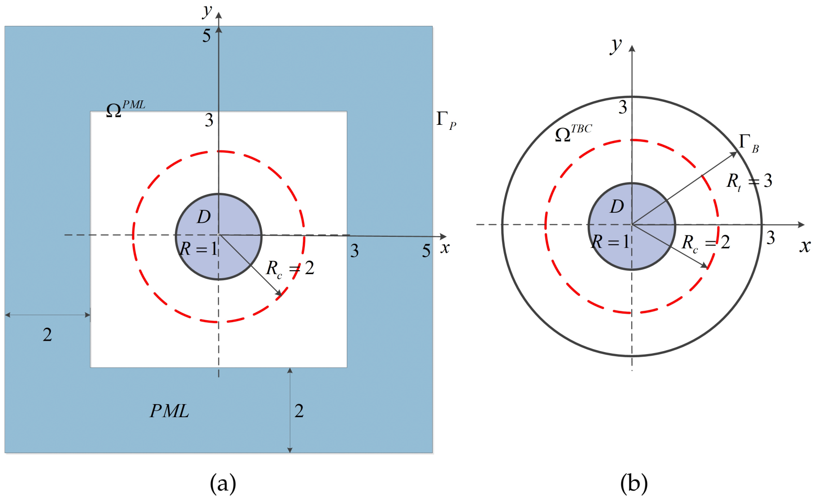

Figure 6: Geometry structure of a circle-shaped obstacle scattering: (a) with the PML truncation; (b) with the TBC truncation.

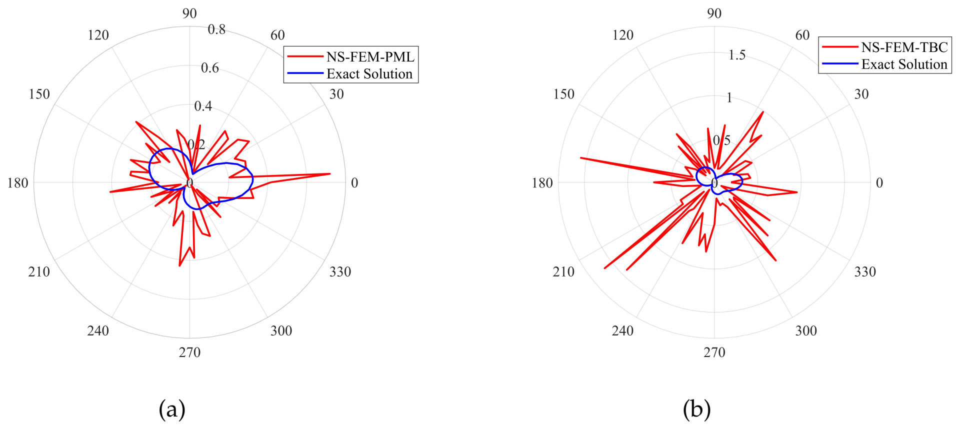

Figure 7: The magnitude of potentials obtained using NS-FEM model at angular frequency : (a) with PML technique; (b) with TBC technique (at mesh $h=0.22$).

5.1.1 Accuracy of numerical solutions

The accuracy and stability of the NS-FEM-L with PML and TBC at different angular frequencies will be discussed. In this numerical example, the characteristic length of mesh h is 0.22, which generates a mesh with 3583 nodes and 6954 elements for PML domain, and a mesh with 968 nodes and 1828 elements for TBC domain. Several different angular frequencies are used to discuss the effect on the accuracy of solutions. Fig. 8 shows the relative errors of potentials ϕ, ψ and scattered field v_1, v_2 on the circle with radius $r=2$

Table 1: These parameters about the obstacle, PML and TBC.

Type	Parameters	Symbols	Values
Circle-shaped obstacle	The radius of circle-shaped obstacle	R	1
	The radius of compare circle	R_c	2
	Lame constants	λ	2
		μ	1
	The incident angle	φ	0
PML	The PML interior boundaries	$x_{\min}=y_{\min}$	3
	The PML outer boundaries	$x_{\max}=y_{\max}$	5
	The parameters of PML functions	$\sigma_1=\sigma_2$	20
	The thickness of the PML	$d_x=d_y$	2
TBC	The radius of TBC	R_t	3
	The truncated number of TBC series	N	30

obtained by using FEM-PML, FEM-TBC, NS-FEM-L-TBC and NS-FEM-L-PML models.

From these results, we find the following some conclusions:

1) For the FEM-PML and FEM-TBC models, the relative errors of potentials ϕ, ψ and scattered field v_1, v_2 have the same trend. The relative errors of ϕ, ψ, (v_1, v_2) decrease for $\omega<0.75\pi$, ($\omega<0.5\pi$) and increase for $\omega>0.75\pi$, ($\omega>0.5\pi$), with the angular frequency increasing. Hence, the minimum relative errors of potentials are 0.059 for FEM-PML, 0.047 for FEM-TBC models and those of scattered field are 0.090 for FEM-PML, 0.088 for FEM-TBC, which are obtained at $\omega=0.75\pi$ and $\omega=0.5\pi$, respectively.

2) For NS-FEM-L-PML and NS-FEM-L-TBC models, as the angular frequencies in-

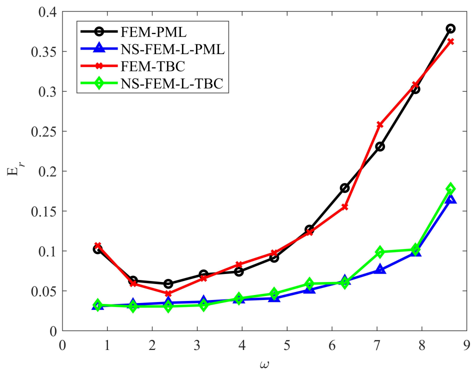

(a)

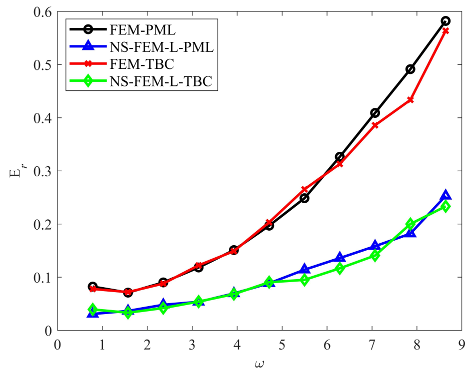

(b)

Figure 8: The relative errors of different models with the angular frequency by a circle-shaped obstacle scattering: (a) potentials ϕ,ψ; (b)scattered field v_1,v_2.

Table 2: The relative errors at circle $r=2$ for mesh size $h=0.22$.

	Agular frequency	Compressional potential ϕ	Shear potential ψ	Scattered field $\boldsymbol{v}=(v_1,v_2)$
FEM-PML	$\omega=\pi$	0.0416	0.1459	0.1337
FEM-TBC		0.0360	0.1067	0.1224
NS-FEM-L-PML		0.0293	0.0607	0.0596
NS-FEM-L-TBC		0.0243	0.0454	0.0542
FEM-PML	$\omega=2\pi$	0.0769	0.3506	0.3104
FEM-TBC		0.0721	0.2913	0.3131
NS-FEM-L-PML		0.0516	0.1098	0.1316
NS-FEM-L-TBC		0.0482	0.0879	0.1168

crease, the relative errors of solutions (potentials and scattered field) become deteriorate gradually. The minimum relative errors of potentials are 0.031 for NS-FEM-L-PML and 0.032 for NS-FEM-L-TBC, and these of scattered field are 0.031 for NS-FEM-L-PML and 0.039 for NS-FEM-L-TBC.

3) Compared to the FEM-PML and FEM-TBC models, the proposed models can obtain more accurate solutions for potentials and scattered field. In addition, the NS-FEM-L model is less sensitive to the wavenumber.

The relative errors of different models for the potentials (compressional and shear potential) and scattered field on the circle $r=2$ at $\omega=\pi$ and $\omega=2\pi$ are listed in Table 2. Fig. 9 and Fig. 10 show the real and imaginary part of solutions at $\omega=2\pi$, respectively.

From the table and figures, we can see that:

1) For the same angular frequency and mesh, the error of compressional potential is smaller than that of shear potential. This can also be easily seen from Fig. 9. This is due to that the shear wavenumber is greater than the compressional at the same angular frequency. It also indicates that the error of coupled Helmholtz equations is mainly caused by shear potential.

2) From the error data and figures of potentials and scattered field, it is clearly seen that numerical solutions of two NS-FEM-L models are closer to analytical solution. This suggests that the NS-FEM-L models are effective for this kind of scattering problem.

5.1.2 Convergence of numerical solutions

The convergence of NS-FEM-L-PML and NS-FEM-LTBC models will be considered at different mesh density for this problem. In this calculation, the angular frequency is fixed to 2π, and several different mesh models are generated by Matlab. Table 3 and Table 4 list the number of nodes and elements of meshes for the PML and TBC problem domains, respectively. From this table, we find that the degree of freedoms (Dofs) of the PML

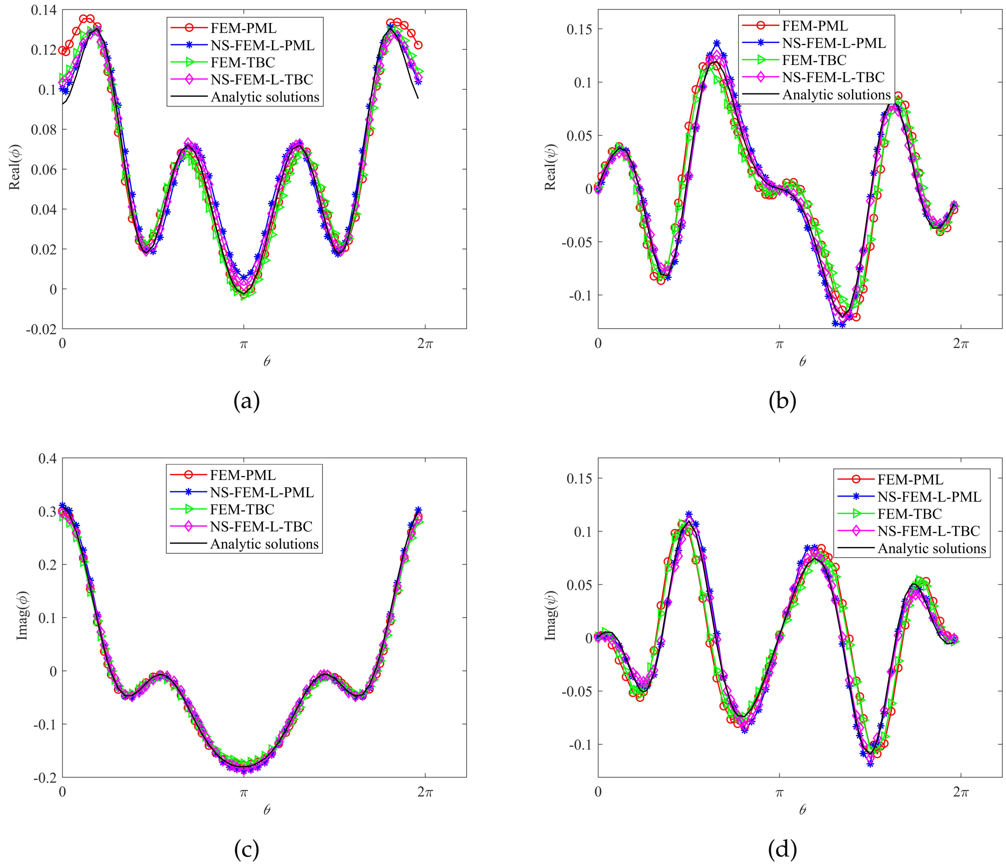

Figure 9: The potentials obtained using different models at $\omega=\pi$ by a circle-shaped obstacle scattering: (a) $\mathrm{Re}(\phi)$; (b) $\mathrm{Re}(\psi)$; (c) $\mathrm{Im}(\phi)$; (d) $\mathrm{Im}(\psi)$ (at mesh $h=0.22$).

Table 3: The meshes for PML problem domain (circle-shaped obstacle).

Mesh	Characteristic length of mesh	Total number of nodes	Total number of elements	Number of nodes on the obstacle and PML boundary		
				Obstacle	PML interior boundary	PML outer boundary
M1	0.40	1055	1990	16	62	104
M2	0.35	1358	2580	20	75	116
M3	0.30	1886	3612	24	84	136
M4	0.25	2668	5144	28	97	164
M5	0.20	4124	8012	32	124	204

problem domain is more than that of the TBC problem domain at the same characteristic length of triangular element for solving the elastic wave scattering problem.

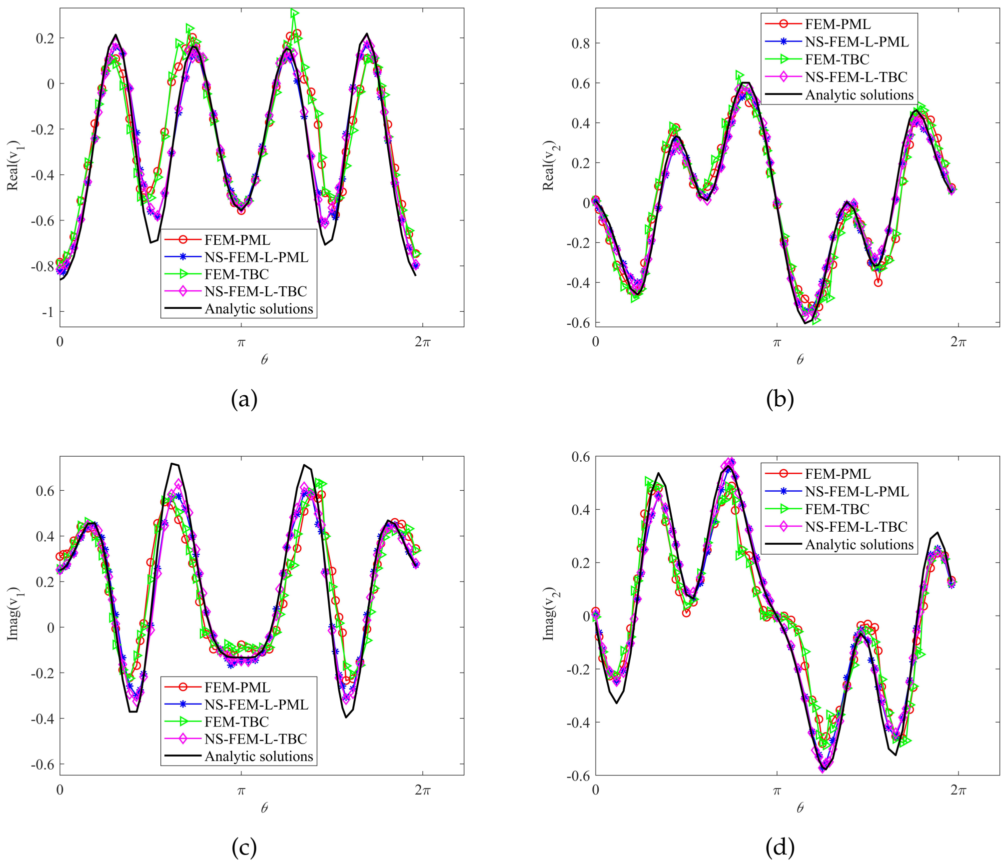

Figure 10: The potentials obtained using different models at $\omega=2\pi$ by a circle-shaped obstacle scattering: (a) $\mathrm{Re}(\phi)$; (b) $\mathrm{Re}(\psi)$; (c) $\mathrm{Im}(\phi)$; (d) $\mathrm{Im}(\psi)$ (at mesh $h=0.22$).

Table 4: The meshes for TBC problem domain (circle-shaped obstacle).

Mesh	Characteristic length of mesh	Total number of nodes	Total number of elements	Number of nodes on the obstacle and TBC boundary	
				Obstacle	TBC
M1	0.40	290	516	16	48
M2	0.35	373	670	20	56
M3	0.30	518	948	24	64
M4	0.25	714	1324	28	76
M5	0.20	1111	2094	32	96
M6	0.15	2003	3834	44	128

1) **The PML problem domain**

The convergence behavior of solutions (L^2 norm and H^1 semi-norm errors) for the

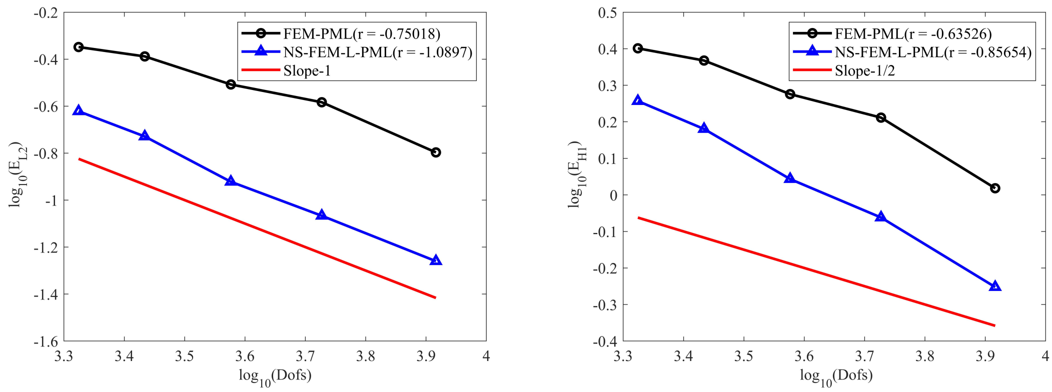

(a) (b)

Figure 11: The convergence behavior from different models with PML for potentials by circle-shaped obstacle scattering: (a) L^2 error; (b) H^1 semi-norm error.

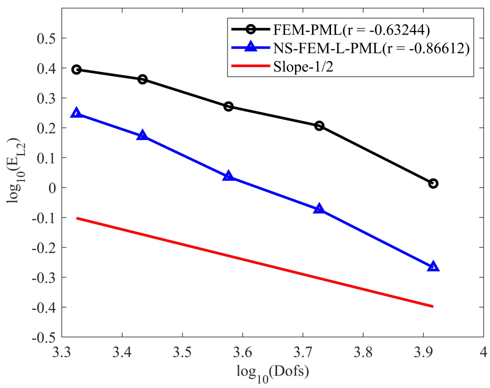

Figure 12: The convergence rate of L^2 error from different models with PML for scattered field by circle-shaped obstacle scattering.

NS-FEM-L-PML method is considered, which is compared with the FEM-PML model. Fig. 11(a) and Fig. 12 show the convergence rate of L^2 error for potentials and scattered field with the Dofs for the FEM-PML and NS-FEM-L-PML models at the angular frequency $\omega=2\pi$. Fig. 11(b) displays the H^1 semi-norm error of potentials against Dofs. It is clear from these figures that the convergence rates (L^2, H^1) of NS-FEM-L-PML ($r=-1.0897$, $r=-0.85654$) are better than the FEM-PML ($r=-0.75018$, $r=-0.63526$) for potentials, and the L^2 error convergence rate of NS-FEM-L-PML ($r=-0.86612$) is better than the FEM-PML ($r=-0.63244$) for scattered field, and the solution errors of two models decrease with mesh refining. In addition, it is found that the H^1 error convergence rate of the potentials is comparable to that of the L^2 error of the scattered field. The reason is that the scattered field is transformed from the divergence and gradient of the potentials in Eq. (2.9) in this paper. From these figures, we can also find that the errors of NS-FEM-L model are smaller at the same mesh.

These results indicate that NS-FEM-L-PML can obtain higher accuracy of solutions and the convergence behavior is better than FEM.

2) **The TBC problem domain**

Next, the convergence behavior of NS-FEM-L-TBC model is considered for this problem, which is compared with the FEM-TBC model. The angular frequency is set to 2π. Fig. 13(a) and Fig. 14 show the convergence of L^2 error for potentials and scattered field with the Dofs for the FEM-TBC and NS-FEM-L-TBC models. Fig. 13(b) shows the H^1 semi-norm error versus the logarithm of Dofs. Fig. 13(a) and Fig. 14 show that the L^2 error convergence rate of the NS-FEM-L-TBC ($r=-0.84606$, $r=-0.79914$) is better than that of the FEM-TBC ($r=-0.7625$, $r=-0.677$) for potentials and scattered field; the H1 semi-norm error convergence rate of the NS-FEM-L-TBC ($r=-0.79757$) is also better than that of the FEM-TBC ($r=-0.67553$) for potentials. This result also verifies that the H^1 semi-norm error of potentials is consistent with the L^2 error of scattered field. These results suggest that the convergence property of the proposed method is better than that of the FEM-TBC for this scattering problem. Meanwhile, NS-FEM-L-TBC model can obtain higher accuracy of solutions.

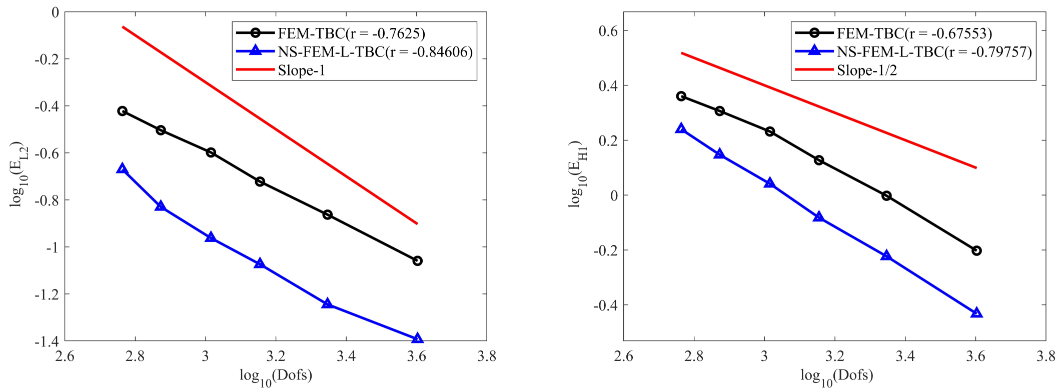

(a) (b)

Figure 13: The convergence behavior from different models with TBC for potentials by circle-shaped obstacle scattering: (a) L^2 error;(b) H^1 semi-norm error.

5.2 Scattering by the elliptical obstacle

The scattering problem by an elliptical obstacle is studied in the subsection. Fig. 15 shows the truncated domains with PML and TBC for an elliptical obstacle. The related parameters for PML and TBC and material parameters are the same as those of Section 5.1.

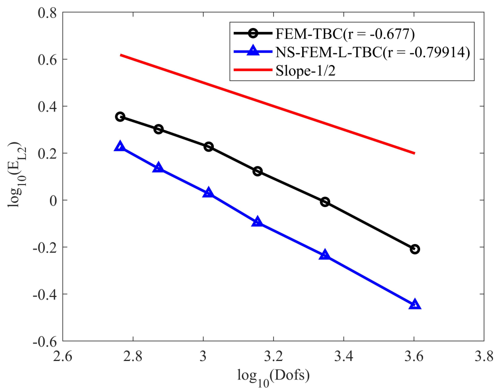

Figure 14: The convergence rate of L^2 error from different models with TBC for scattered field by circle-shaped obstacle scattering.

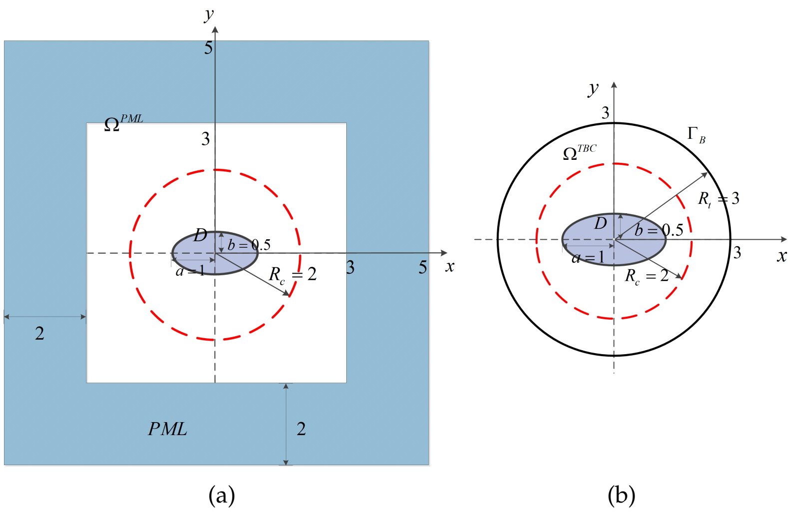

Figure 15: Geometry structure of an ellipse-shaped obstacle scattering: (a) with the PML truncation; (b) with the TBC truncation.

The incident wave is a compressional wave, and the incident angle is 0. The parametric equations of the obstacle boundary are

$$x(t)=\cos(t), \quad y(t)=0.5\sin(t), \tag{5.4}$$

where the parameter $t\in[0\ 2\pi]$. For the convenience of comparison, the reference solution is obtained by using Freefem++ software and taking the continuous piecewise quadratic function as the basis function. Besides, all meshes in this experiment are generated by Freefem++ software.

5.2.1 Accuracy of numerical solutions

The accuracy of solutions by the NS-FEM-L with PML and TBC for the elliptical obstacle scattering at different angular frequencies are discussed in this sub-section. In this experiment, the mesh is fixed. The PML model includes 7437 nodes and 14464 elements, where the characteristic length is 0.16. The TBC model includes 2552 nodes and 4834 elements, where the characteristic length is 0.145. Fig. 16 shows the relative errors of numerical solutions (ϕ, ψ and v_1, v_2) on the circle $r=2$ with different angular frequencies. The circle sets 90 nodes for PML and TBC models. From the above results, the following can be found:

1) For the two FEM models, the numerical errors at small angular frequency ($\omega \in [0.25\pi, 0.75\pi]$) are relatively large, and then the errors increase as the angular frequency increases. For the NS-FEM-L models, both NS-FEM-L-PML and NS-FEM-L-TBC models increase as angular frequency increases. Moreover, the solution of two NS-FEM-L models also keeps a small error at small angular frequency. These results indicate that two NS-FEM-L models are not very sensitive to angular frequency;

2) For the same mesh and angular frequency, it can be found that the error of the proposed method is smaller than that of FEM, which shows that NS-FEM-L model is more stable.

To compare the numerical solutions of different models more clearly, the magnitudes of potentials and scattered field ($\omega = 2\pi$) are plotted in Fig. 17 and Fig. 18. The mesh consists of 4049 nodes and 7798 elements for PML problem domain, and its characteristic length is 0.22; the mesh includes 1486 nodes and 2786 elements for TBC problem domain

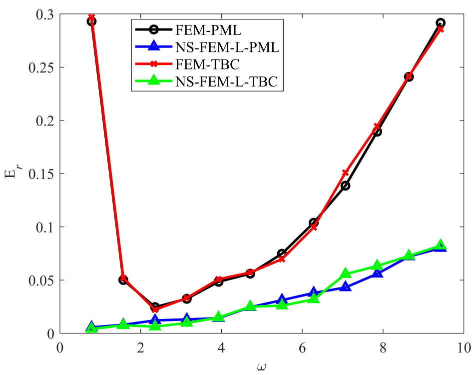

(a)

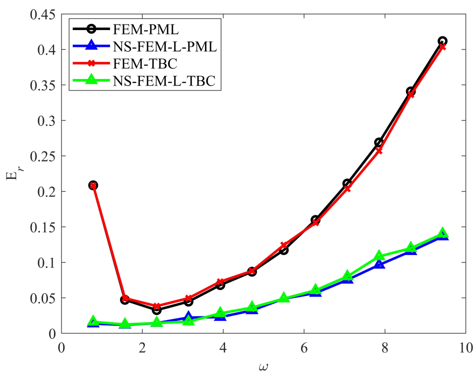

(b)

Figure 16: The relative errors of different models with the angular frequency by an ellipse-shaped obstacle: (a) potentials ϕ, ψ; (b) scattered field v_1, v_2.

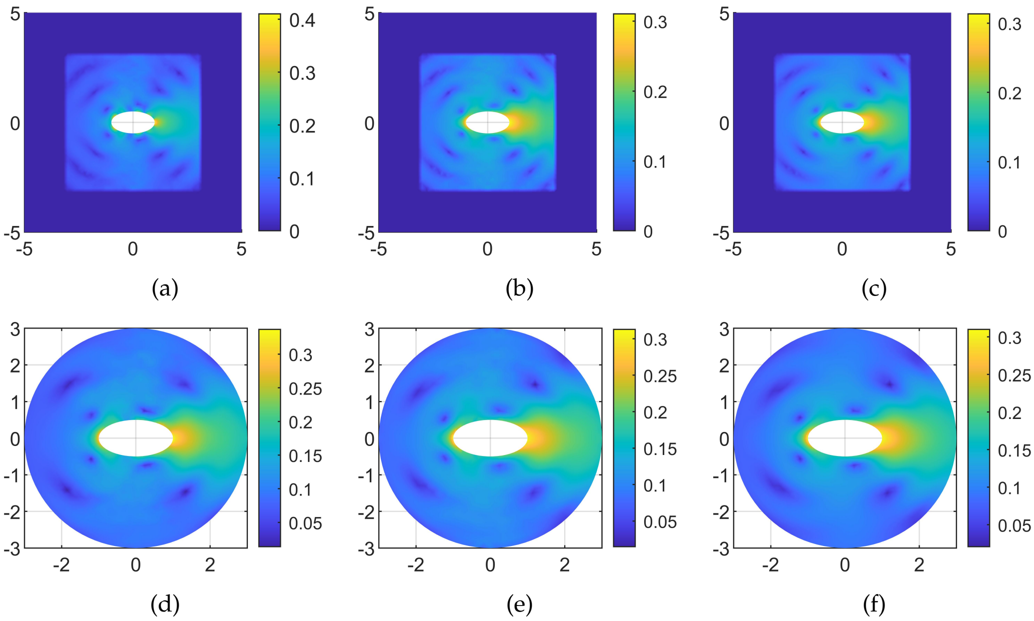

Figure 17: The magnitudes of potentials obtained using different models by an elliptical obstacle: (a) FEM-PML; (b) NS-FEM-L-PML; (c) reference solutions (PML); (d) FEM-TBC; (e) NS-FEM-L-TBC; (f) reference solutions (TBC).

and its characteristic length is 0.19. From these figures, we can observe that the solution of NS-FEM-L model is closer to reference solution than that of FEM model, regardless of PML or TBC techniques. These results also show that the solutions of NS-FEM-L models have high accuracy and stability.

5.2.2 Convergence of numerical solutions

The convergence behavior of numerical solutions by NS-FEM-L with PML and TBC for the elliptical obstacle scattering are considered in this sub-section. The angular frequency is taken as 2π and the meshes that generated by Freefem++ software are used for convergence analysis. The numbers of nodes and elements in PML and TBC problem domains are listed in Table 5 and Table 6, respectively.

1) **The PML problem domain**

The convergence behavior of NS-FEM-L-PML and FEM-PML models are analyzed in this subsection. Fig. 19 shows the convergence rate of potentials, including L^2 error and H^1 semi-norm error, respectively. Fig. 20 shows the convergence rate of L^2 error for the scattered field. From Fig. 19(a) and Fig. 20, we can see that the convergence rates of L^2 error of the NS-FEM-L-PML model ($r=-1.2236$, $r=-0.98214$) are better than that of the FEM-PML ($r=-0.88437$, $r=-0.76526$). It can be found from Fig. 19(b) and Fig. 20 that the convergence rate of L^2 error of the scattered field ($r=-0.988$, $r=-0.78299$) is

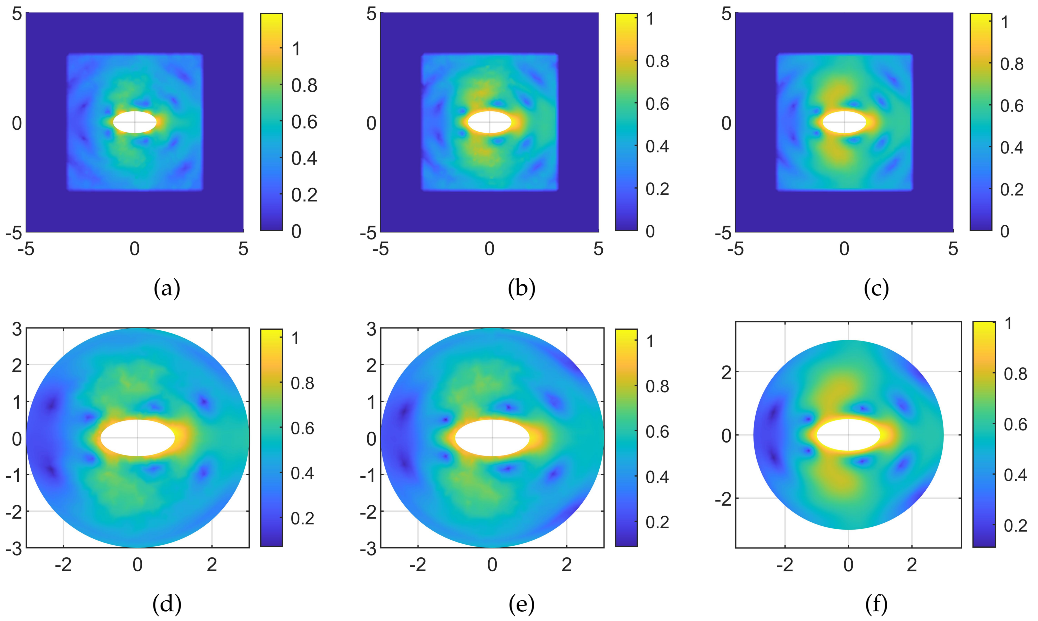

Figure 18: The magnitudes of scattered field obtained using different models by an elliptical obstacle: (a) FEM-PML; (b) NS-FEM-L-PML; (c) reference solutions (PML); (d) FEM-TBC; (e) NS-FEM-L-TBC; (f) reference solutions (TBC).

Table 5: The meshes for PML problem domain (ellipse-shaped obstacle).

Mesh	Characteristic length of mesh	Total number of nodes	Total number of elements	Number of nodes on the obstacle and PML boundary		
				Obstacle	PML interior boundary	PML outer boundary
M1	0.35	1625	3098	24	96	128
M2	0.27	2772	5352	32	128	160
M3	0.22	4196	8160	40	160	192
M4	0.18	5893	11514	48	192	224

Table 6: The meshes for TBC problem domain (ellipse-shaped obstacle).

Mesh	Characteristic length of mesh	Total number of nodes	Total number of elements	Number of nodes on the obstacle and TBC boundary	
				Obstacle	TBC
M1	0.30	585	1074	24	72
M2	0.23	1003	1878	32	96
M3	0.18	1591	3022	40	120
M4	0.15	2305	4418	48	144

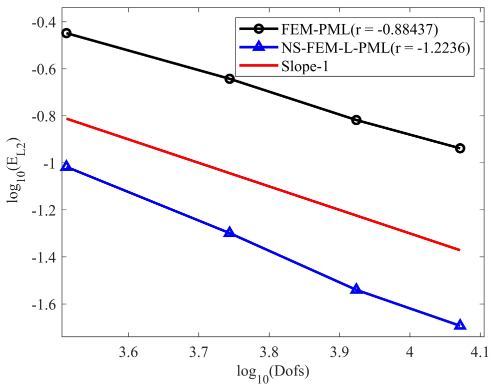

(a)

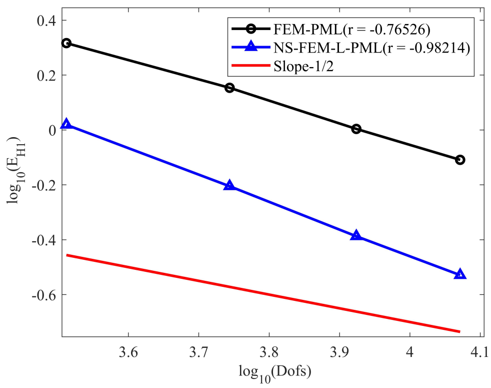

(b)

Figure 19: The convergence behavior from different models with PML for potentials by ellipse-shaped obstacle scattering: (a) L^2 error; (b) H^1 semi-norm error.

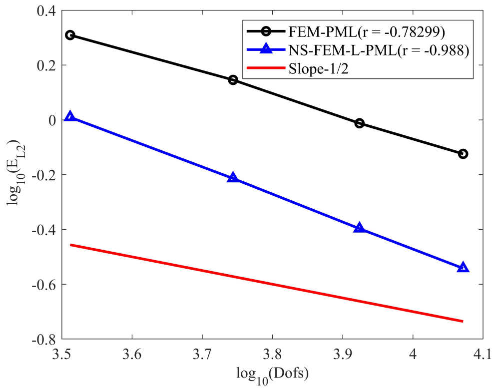

Figure 20: The convergence rate of L^2 error from different models with PML for scattered field by ellipse-shaped obstacle scattering.

consistent with the convergence rate of H^1 semi-norm error of potentials ($r=-0.98214$, $r=-0.76526$). Besides, these figures also show that the numerical errors (L^2 error, H^1 semi-norm error) of NS-FEM-L-PML model is smaller at the same degree of freedoms. These conclusions suggest that the NS-FEM-L-PML model is an effective numerical method for solving scattering problems.

2) **The TBC problem domain**

The convergence behavior of the NS-FEM-L-TBC model is considered in this subsection. Fig. 21 shows the convergence rates of L^2 error and H^1 semi-norm error for potentials. The convergence rates of L^2 error and H^1 semi-norm error are -1.2695, -0.86705

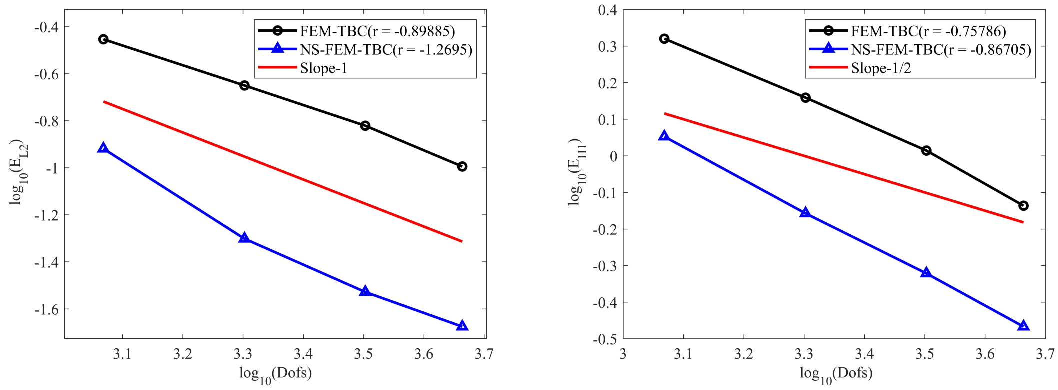

(a) (b)

Figure 21: The convergence behavior from different models with TBC for potentials by ellipse-shaped obstacle scattering: (a) L^2 error; (b) H^1 semi-norm error.

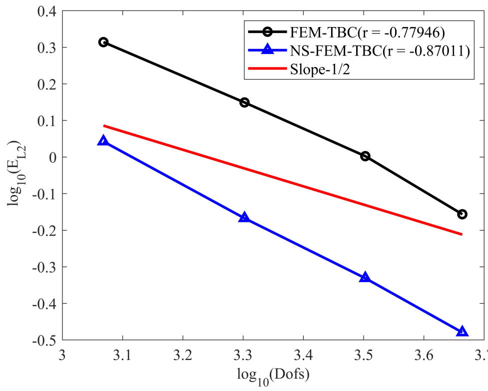

Figure 22: The convergence rate of L^2 error from different models with TBC for scattered field by ellipse-shaped obstacle scattering.

for NS-FEM-L-TBC model, which are higher than FEM-TBC model ($r=-0.89885$, $r=-0.75786$). The L^2 convergence rate of scattered field is shown in Fig. 22. The convergence rate of H^1 semi-norm error for scattered field ($r=-0.87011$, $r=-0.77946$) is basically the same as the L^2 convergence rate of the potentials by using the two models. Form these figures, it is clearly seen that the NS-FEM-L-TBC model can obtain high accuracy and better convergence rate.

5.3 Scattering by the acorn-shaped obstacle

The scattering problem by an acorn-shaped obstacle will be considered in the subsection. The parameters of PML and TBC are the same as Example 1, the problem domains are

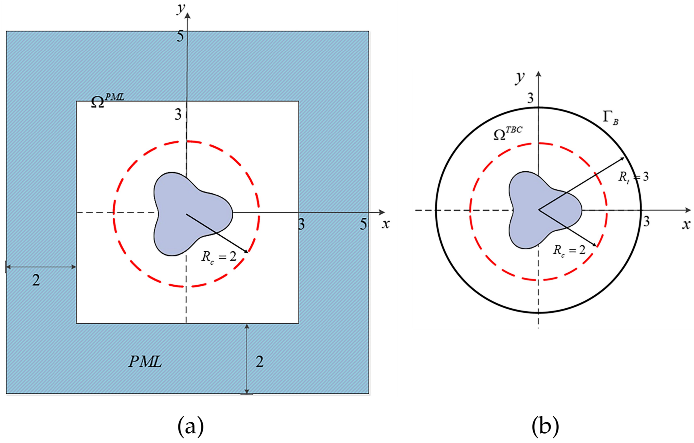

Figure 23: Geometry structure of an acorn-shaped obstacle scattering: (a) with the PML truncation; (b) with the TBC truncation.

shown in Fig. 23. The incident wave is same as in Section 5.2. The parametric equations for this acorn-shaped obstacle boundary are

$$x(t)=\cos(t)(1+0.25\cos(3t)), \quad y(t)=\sin(t)(1+0.25\cos(3t)), \tag{5.5}$$

where the parameter $t\in[0,\ 2\pi]$. In this example, the reference solution is obtained by Freefem++ software, where the basis function is the continuous piecewise quadratic function. Besides, all meshes in this experiment are generated by Freefem++ software.

5.3.1 Accuracy of numerical solutions

The accuracy of solutions of different models for the acorn-shaped obstacle scattering at different angular frequencies is studied in this sub-section. In this calculation, several different angular frequencies are selected and the mesh is fixed. Both PML and TBC problem domains have 100 points on the obstacle and the circle of comparison. For PML model, the mesh is discretized by setting 160 points on inner boundary and 200 points on outer boundary of PML, which includes 5190 nodes and 10040 elements. For TBC model, the mesh is discretized by setting 150 points on the TBC boundary, which includes 2186 nodes and 4122 elements. Fig. 24 shows the relative errors of the potentials and scattered field at different angular frequencies, where the error on the red curve in Fig. 23 is calculated. From the results, the following can be observed:

1) For both PML and TBC models, the numerical solution of FEM is greatly affected by the angular frequency, and its overall error is higher than that of NS-FEM-L model. Besides, the error growth rate of NS-FEM-L models are much smaller than that of FEM. It also shows that the NS-FEM-L model is stable.

2) The accuracy of the solution of the scattered field is not as high as that of the potentials. The reason is that the scattered field is obtained by the transformation of

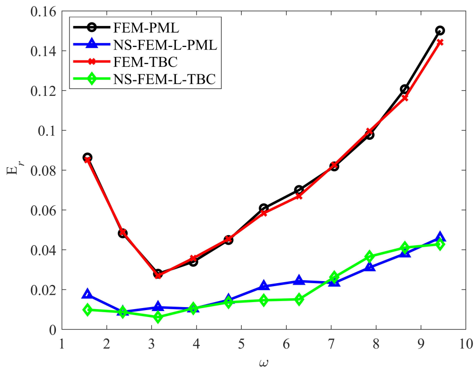

(a)

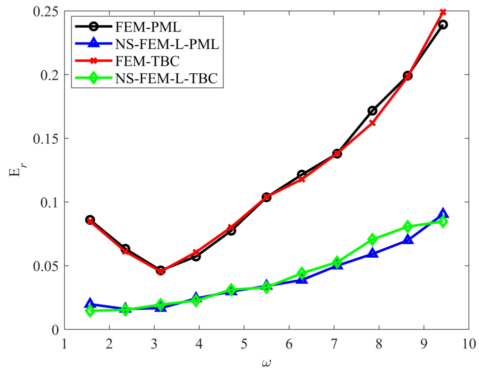

(b)

Figure 24: The relative errors of different models with the angular frequency by an acorn-shaped obstacle: (a) potentials ϕ, ψ; (b) scattered field v_1, v_2.

the solution of the potentials through curl and gradient operator in Eq. (2.9), which leads to certain errors.

Next, we study the magnitudes of the numerical solutions for different models at angular frequency, as shown in Fig. 25 and Fig. 26. For the PML problem domain, the mesh contains 2126 nodes and 4034 elements, where there are 50 nodes on the obstacle, 100 nodes on the PML inner boundary and 168 nodes on the PML outer boundary. For TBC, the mesh consists of 1034 nodes and 1918 elements, with 50 nodes on the obstacle and 75 nodes on the TBC boundary. From these results, it can see that the NS-FEM-L model can obtain better solutions, especially near the obstacle boundary. It also suggests that NS-FEM-L model can solve the problem more effectively.

5.3.2 Convergence of numerical solutions

In this sub-section, the convergence of numerical solutions by the NS-FEM-L-TBC models are studied for the acorn-shaped obstacle scattering with fixed angular frequency 2π. Table 7 and Table 8 list the mesh information of PML and TBC problem domains.

1) **The PML problem domain**

Firstly, the convergence behavior of PML problem by using NS-FEM-L-PML and FEM-PML models is studied. Fig. 27(a) and Fig. 28 show the convergence results for potentials and scattered field according to the L^2 error versus the Dofs, respectively. From these figures, it can be observed that the convergence rates of L^2 error of NS-FEM-L-PML model ($r=-1.2055$, $r=-0.95929$) are high than that of FEM-PML ($r=-0.83852$, $r=-0.77368$) for potentials and scattered field. Fig. 27(b) plots the convergence result with respect to H^1 semi-norm error of potentials. The results indicate that NS-FEM-L-PML model ($r=-0.95831$) converges faster than FEM-PML model ($r=-0.64669$). All

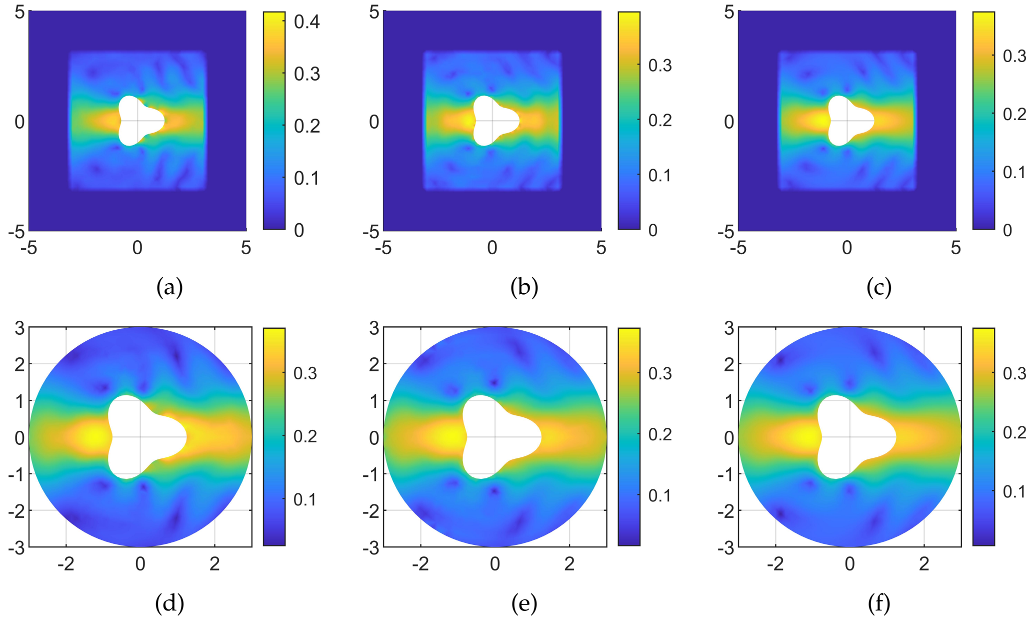

Figure 25: The magnitudes of potentials obtained using different models by an acorn-shaped obstacle: (a) FEM-PML; (b) NS-FEM-L-PML; (c)reference solutions (PML); (d) FEM-TBC; (e) NS-FEM-L-TBC; (f) reference solutions (TBC).

Table 7: The meshes for PML problem domain (acorn-shaped obstacle).

Mesh	Characteristic length of mesh	Total number of nodes	Total number of elements	Number of nodes on the obstacle and PML boundary		
				Obstacle	PML interior boundary	PML outer boundary
M1	0.36	1437	2702	40	80	132
M2	0.30	2126	4034	50	100	168
M3	0.22	4207	8124	70	140	220
M4	0.17	6855	16460	90	180	300

Table 8: The meshes for TBC problem domain (acorn-shaped obstacle).

Mesh	Characteristic length of mesh	Total number of nodes	Total number of elements	Number of nodes on the obstacle and TBC boundary	
				Obstacle	TBC
M1	0.32	466	832	40	60
M2	0.26	731	1337	50	75
M3	0.19	1386	2597	70	90
M4	0.15	2262	4299	90	135

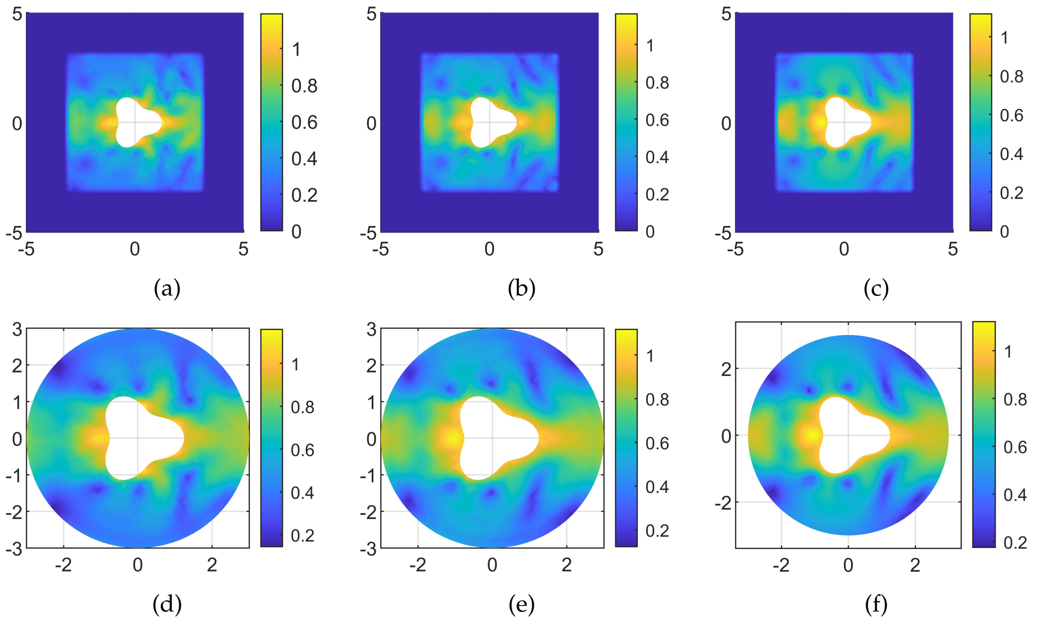

Figure 26: The magnitudes of scattered field obtained using different models by an acorn-shaped obstacle: (a) FEM-PML; (b) NS-FEM-L-PML; (c) reference solutions (PML); (d) FEM-TBC; (e) NS-FEM-L-TBC; (f) reference solutions (TBC).

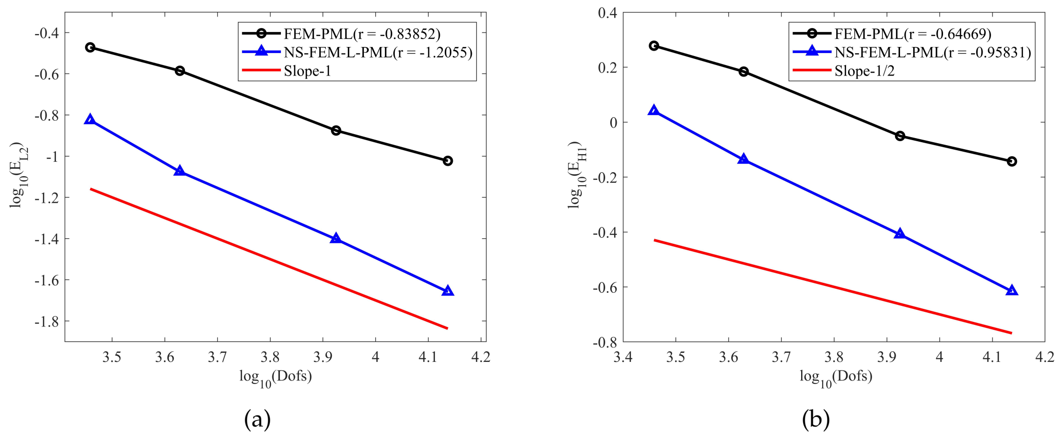

Figure 27: The convergence behavior from different models with PML for potentials by acorn-shaped obstacle scattering: (a) L^2 error; (b) H^1 semi-norm error.

these conclusions indicate that the NS-FEM-L-PML model is superior to the FEM-PML model.

2) **The TBC problem domain**

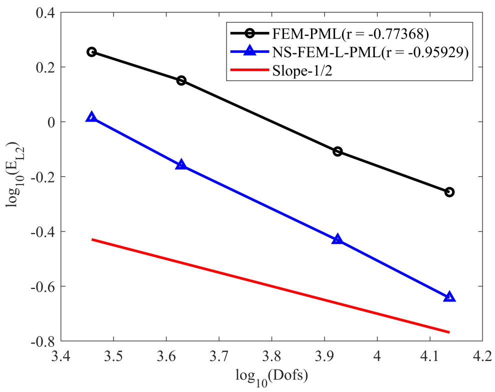

Figure 28: The convergence rate of L^2 error from different models with PML for scattered field by acorn-shaped obstacle scattering.

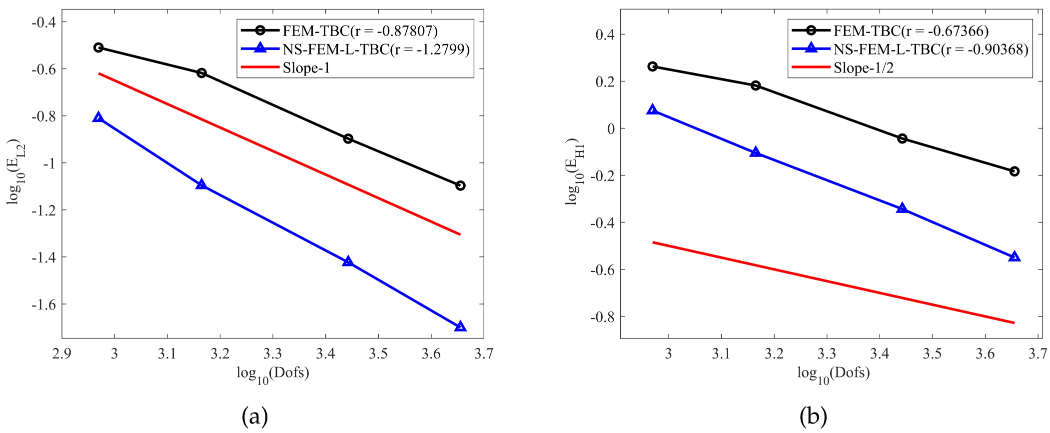

Figure 29: The convergence behavior from different models with TBC for potentials by acorn-shaped obstacle scattering:(a)L^2 error;(b)H^1 semi-norm error.

Then, the convergence behavior of TBC method is discussed in this subsection. Fig. 29 shows the convergence rates of L^2 and H^1 semi-norm errors for potentials versus the logarithm of Dofs. The convergence rate of L^2 error of scattered field is shown in Fig. 30. From these figures, the following can be observed:

1) The convergence rates (L^2, H^1) of the NS-FEM-L-TBC model for potentials ($r=-1.2799$, $r=-0.90368$) are higher than those of the FEM-TBC ($r=-0.87807$, $r=-0.67366$), and the error is smaller at the same mesh.

2) The NS-FEM-L-TBC model can provide better convergence rate ($r=-0.91235$) than FEM-TBC ($r=-0.78716$) for scattered field.

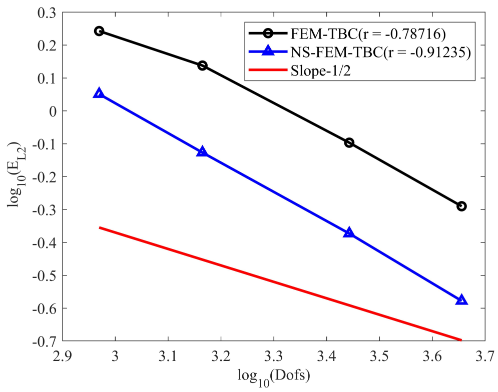

Figure 30: The convergence rate of L^2 error from different models with TBC for scattered field by acorn-shaped obstacle scattering.

In conclusion, these results indicate that NS-FEM-L-TBC model is more effective and accurate than FEM model for solving this scattering problem.

Appendix: The uniqueness of Helmholtz decomposition

In the section, we give a brief illustration of Remark 2.1. Firstly, we apply TBC on the appropriate boundary, and obtain the following boundary value problem of the total field $\boldsymbol{u}$ ($\boldsymbol{u}=\boldsymbol{v}+\boldsymbol{u}^{inc}$)

$$\begin{cases} \mu\Delta\boldsymbol{u}+(\lambda+\mu)\nabla\nabla\cdot\boldsymbol{u}+\omega^2\boldsymbol{u}=0 & \text{in } \Omega, \\ \boldsymbol{u}=0 & \text{on } \Gamma_D, \\ \mathscr{B}\boldsymbol{u}=\mathscr{T}\boldsymbol{u}+\boldsymbol{g} & \text{on } \Gamma_B, \end{cases} \tag{A.1}$$

where

$$\boldsymbol{g}:=\mathscr{B}\boldsymbol{u}^{inc}-\mathscr{T}\boldsymbol{u}^{inc} \quad \text{and} \quad \mathscr{B}\boldsymbol{u}=\mu\partial_r\mathbf{u}+(\lambda+\mu)\nabla\cdot\boldsymbol{v}\boldsymbol{e}_r,$$

in which $\boldsymbol{e}_r$ is the unit outward normal vector on Γ_B. It is shown in [3] that the scattered field satisfies the transparent boundary condition on Γ_B

$$\mathscr{B}\boldsymbol{v}=\mathscr{T}\boldsymbol{v}=\sum_{n\in\mathbb{Z}} M_n\boldsymbol{v}^{(n)}e^{\mathrm{i}n\theta}, \quad \boldsymbol{v}=\sum_{n\in\mathbb{Z}}\boldsymbol{v}^{(n)}e^{\mathrm{i}n\theta},$$

where M_n is a $2*2$ matrix.

Because TBCs are derived from the sommerfeld conditions, we have the following Remark.

Remark A.1. The problem (2.2)-(2.4) is equivalent to the TBC truncated problem (A.1) and the problem (2.6)-(2.8) is equivalent to the TBC truncated problem (2.6), (2.7) and (2.18).

Combined with above Remark, we need to illustrate the uniqueness of Helmholtz decomposition through the well-posedness of truncated problems (A.1) and (2.6), (2.7), (2.18) to demonstrate Remark 2.1. See the following Remark for details.

Remark A.2. Let $\boldsymbol{v}=\boldsymbol{u}-\boldsymbol{u}^{inc}$ be the scattered field corresponding to the solution $\boldsymbol{u}$ of the boundary value problem (A.1). Then the scattered field $\boldsymbol{v}$ can be decomposed using the Helmholtz decomposition $\boldsymbol{v}=\nabla\phi+\mathbf{curl}\psi$, where $\phi=-\kappa_p^{-2}\nabla\cdot\boldsymbol{v}$, $\psi=\kappa_s^{-2}curl\boldsymbol{v}$ are the solutions of the coupled boundary value problem (2.6), (2.7), (2.18), and the Helmholtz decomposition is unique.

Proof. Let $\boldsymbol{v}=\boldsymbol{u}-\boldsymbol{u}^{inc}$ be the scattered field corresponding to the solution $\boldsymbol{u}$ of the boundary value problem (A.1), which is proved by its variational formulation in of [3, Theorem 3.10].

According to the relationship between scalar and vector curl operators, we can obtain

$$\mathbf{curl}curl\boldsymbol{v}=-\Delta\boldsymbol{v}+\nabla\nabla\cdot\boldsymbol{v}. \tag{A.2}$$

Divide both sides of the Navier equation of the scattered field $\boldsymbol{v}$ by ω^2, and then combine with the above relationship, the Eq. (2.2) can be re-written as

$$-\kappa_s^{-2}\mathbf{curl}curl\boldsymbol{v}+\kappa_p^{-2}\nabla\nabla\cdot\boldsymbol{v}+\boldsymbol{v}=0. \tag{A.3}$$

Let

$$\boldsymbol{v}_p:=-\kappa_p^{-2}\nabla\nabla\cdot\boldsymbol{v},\quad \boldsymbol{v}_s:=\kappa_s^{-2}\mathbf{curl}curl\boldsymbol{v}. \tag{A.4}$$

Then Eq. (A.3) becomes

$$\boldsymbol{v}=\boldsymbol{v}_p+\boldsymbol{v}_s. \tag{A.5}$$

It is clear that $\boldsymbol{v}_p$ and $\boldsymbol{v}_s$ satisfy

$$\mathbf{curl}\boldsymbol{v}_p=0,\quad \nabla\cdot\boldsymbol{v}_s=0. \tag{A.6}$$

From Eqs. (A.4)-(A.6), we can get

$$\nabla\nabla\cdot\boldsymbol{v}_p+\kappa_p^2\boldsymbol{v}_p=0,\quad \Delta\boldsymbol{v}_s+\kappa_s^2\boldsymbol{v}_s=0. \tag{A.7}$$

If we take

$$\phi:=-\kappa_p^{-2}\nabla\cdot\boldsymbol{v},\quad \psi:=\kappa_s^{-2}curl\boldsymbol{v}, \tag{A.8}$$

then we have

$$\boldsymbol{v}=\boldsymbol{v}_p+\boldsymbol{v}_s=\nabla\phi+\mathbf{curl}\psi, \tag{A.9}$$

where $\boldsymbol{v}_p=\nabla\phi$ and $\boldsymbol{v}_s=\mathbf{curl}\psi$, which is the Helmholtz decomposition of the scattered field $\boldsymbol{v}$. It is from Eqs. (A.7) and (A.8) that ϕ and ψ satisfy

$$\Delta\phi+\kappa_p^2\phi=0,\quad \Delta\psi+\kappa_s^2\psi=0. \tag{A.10}$$

Similarly, using Eq. (A.9), the boundary condition (2.3) and sommerfeld condition (2.4), we can obtain the following boundary conditions for the potentials

$$\begin{cases} \partial_\nu\phi+\partial_\tau\psi=f, \quad \partial_\nu\psi-\partial_\tau\phi=g \quad \text{on } \Gamma_D, \\ \lim\limits_{\rho\to\infty}\rho^{\frac{1}{2}}(\partial_\rho\phi-\mathrm{i}\kappa_p\phi)=0, \quad \lim\limits_{\rho\to\infty}\rho^{\frac{1}{2}}(\partial_\rho\psi-\mathrm{i}\kappa_s\psi)=0, \quad \rho=|\mathbf{x}|. \end{cases} \tag{A.11}$$

Besides, we can know that the variational problem of (2.6), (2.7), (2.18) has at most one solution from in [3, Theorem 3.5], which implies the solutions $\phi=-\kappa_p^{-2}\nabla\cdot\boldsymbol{v}$, $\psi=\kappa_s^{-2}curl\boldsymbol{v}$ are unique for the truncated potentials problem.

Combined the Remark A.1 with the uniqueness of solution $\boldsymbol{v}$ in problem (A.1) and solutions $\phi=-\kappa_p^{-2}\nabla\cdot\boldsymbol{v}$, $\psi=\kappa_s^{-2}curl\boldsymbol{v}$ in truncated potentials problem, the uniqueness of the Helmholtz decomposition can be obtained. It is clear that Remark 2.1 is hold based on Remarks A.1 and A.2. □

Acknowledgements

The authors was supported by the National Natural Science Foundation of China (Grant Nos. 11901423, 12002290 and 11771321), the Youth Science and the Technology Research Foundation of Shanxi Province (Grant Nos. 201901D211104 and 201901D211107) and the Shanxi Youth Top-Notch Talent Support Program (Grant No. DT18100306).

References

[1] D. Colton and R. Kress, *Integral equation methods in scattering theory,* Society for Industrial and Applied Mathematics, 2013.
[2] D. Colton and R. Kress, Inverse Acoustic and Electromagnetic Scattering Theory, Springer, 1998.
[3] P. Li, Y. Wang, Z. Wang and Y. Zhao, *Inverse obstacle scattering for elastic waves,* Inverse Problems, 32 (2016), p. 115018.
[4] L. Tsang, J. Kong and K. Ding, Scattering of Electromagnetic Waves: Theories and Applications, John Wiley and Sons, 27 (2004).
[5] J. Yue, G. Liu, M. Li and R. Niu, *An edge-based smoothed finite element method for wave scattering by an obstacle in elastic media,* Eng. Anal. Bound. Elem., 101 (2019), pp. 121–138.
[6] Y. Chai, Z. Gong and W. Li et al., *Application of smoothed finite element method to two-dimensional exterior problems of acoustic radiation,* Int. J. Comput. Methods, 15 (2017), p. 1850029.
[7] J. Berenger, *A perfect matched layer for the absorption of electromagnetic waves,* J. Comput. Phys., 114 (1994), pp. 185–200.
[8] J. Bramble and J. Pasciak, *Analysis of a finite PML approximation for the three dimensional time-harmonic maxwell and acoustic scattering problems,* Math. Comput., 76 (2007), pp. 597–614.
[9] T. Hohage, F. Schmidt and Z. Lin, *Solving time-harmonic scattering problems based on the pole condition II: Convergence of the PML method,* SIAM J. Math. Anal., 35 (2003), pp. 547–560.

[10] Z. CHEN AND X. WU, *An adaptive uniaxial perfectly matched layer method for time-harmonic scattering problems,* Numer. Math. Theor. Meth. Appl., 1 (2008), pp. 113–137.

[11] X. JIANG AND P. LI, *An adaptive finite element PML method for the acoustic-elastic interaction in three dimensions,* Commun. Comput. Phys., 22 (2017), pp. 1486–1507.

[12] J. BRAMBLE, J. PASCIAK AND D. TRENEV, *Analysis of a finite PML approximation to the three dimensional elastic wave scattering problem,* Math. Comput., 79 (2010), pp. 2079–2101.

[13] Z. CHEN, X. XIANG AND X. ZHANG, *Convergence of the PML method for elastic wave scattering problems,* Math. Comput., 302 (2016), pp. 2687–2714.

[14] F. HASTINGS, J. SCHNEIDER AND S. BROSCHAT, *Application of the perfectly matched layer (PML) absorbing boundary condition to elastic wave propagation,* J. Acous. Soc. Am., 100 (1996), pp. 3061–3069.

[15] X. JIANG, P. LI AND J. LV ET AL., *An adaptive finite element PML method for the elastic wave scattering problem in periodic structures,* ESAIM: Math. Model. Numer. Anal., 51 (2016), pp. 2017–2047.

[16] X. JIANG, P. LI AND J. LV ET AL., *Convergence of the PML solution for elastic wave scattering by biperiodic structures,* Commun. Math. Sci., 16 (2018), pp. 987–1016.

[17] Z. HE, G. LIU AND Z. ZHONG ET AL., *An edge-based smoothed finite element method (ES-FEM) for analyzing three-dimensional acoustic problems,* Comput. Methods Appl. Mech. Eng., 199 (2009), pp. 20–33.

[18] G. WANG, X. CUI AND Z. LIANG ET AL., *A coupled smoothed finite element method (S-FEM) for structural-acoustic analysis of shells,* Eng. Anal. Bound. Elem., 61 (2015), pp. 207–217.

[19] F. WU, L. YAO AND M. HU ET AL., *A stochastic perturbation edge-based smoothed finite element method for the analysis of uncertain structural-acoustics problems with random variables,* Eng. Anal. Bound. Elem., 80 (2017), pp. 116–126.

[20] Y. CHAI, W. LI AND Z. GONG ET AL., *Hybrid smoothed finite element method for two-dimensional underwater acoustic scattering problems,* Ocean Eng., 116 (2016), pp. 129–141.

[21] W. LI, Y. CHAI AND M. LEI ET AL., *Numerical investigation of the edge-based gradient smoothing technique for exterior Helmholtz equation in two dimensions,* Comput. Struct., 182 (2017), pp. 149–164.

[22] Y. CHAI, Z. GONG AND W. LI ET AL., *Application of smoothed finite element method to acoustic scattering from underwater elastic objects,* J. Acoust. Soc. Am., 141 (2017), pp. 3708–3708.

[23] Y. CHAI, W. LI AND T. LI ET AL., *Analysis of underwater acoustic scattering problems using stable node-based smoothed finite element method,* Eng. Anal. Bound. Elem., 72 (2016), pp. 27–41.

[24] X. HU, X. CUI AND Q. ZHANG ET AL., *The stable node-based smoothed finite element method for analyzing acoustic radiation problems,* Eng. Anal. Bound. Elem., 80 (2017), 142-151.

[25] P. MONK, Finite Element Methods for Maxwell's Equations, Oxford University Press, 2003.

[26] F. IHLENBURG, I. BABUSKA AND S. SAUTER, *Reliability of finite element methods for the numerical computation of waves,* Adv. Eng. Software, 28 (1997), pp. 417–424.

[27] G. LIU AND G. ZHANG, Smoothed Point Interpolation Methods: *G* Space Theory and Weakened Weak Forms, World Scientific, 2013.

[28] G. LIU AND N. TRUNG, Smoothed Finite Element Methods, CRC Press, 2016

[29] G. LIU, *A G space theory and a weakened weak (W2) form for a unified formulation of compatible and incompatible methods: Part I theory,* Int. J. Numer. Methods Eng., 81 (2010), pp. 1093–1126.

[30] J. YUE, M. LI AND G. LIU ET AL., *Proofs of the stability and convergence of a weakened weak method using PIM shape functions,* Comput. Math. Appl., 72 (2016), pp. 933–951.

[31] T. NGUYEN-THOI, H. VU-DO AND T. RABCZUK ET AL., *A node-based smoothed finite element method (NS-FEM) for upper bound solution to visco-elastoplastic analyses of solids using triangular*

and tetrahedral meshes, Comput. Methods Appl. Mech. Eng., 199 (2010), pp. 3005–3027.

[32] G. LIU, L. CHEN AND M. LI, *S-FEM for fracture problems, theory, formulation and application,* Int. J. Comput. Methods, 11 (2014), p. 1343003.

[33] H. NGUYENXUAN, G. LIU AND T. NGUYENTHOI ET AL., *An edge-based smoothed finite element method for analysis of two-dimensional piezoelectric structures,* Smart Mater. Struct., 18 (2009), pp. 5022–5039.

[34] S. WU, G. LIU AND X. CUI ET AL., *An edge-based smoothed point interpolation method (ES-PIM) for heat transfer analysis of rapid manufacturing system,* Int. J. Heat Mass Transf., 53 (2010), pp. 1938–1950.

[35] Z. WU, J. YUE AND M. LI ET AL., *An edge-based smoothed finite element method with TBC for the elastic wave scattering by an obstacle,* Commun. Comput. Phys., 30 (2021), pp. 709–748.

[36] G. LIU, T. NGUYEN-THOI AND H. NGUYEN-XUAN ET AL., *A node-based smoothed finite element method (NS-FEM) for upper bound solutions to solid mechanics problems,* Comput. Struct., 87 (2009), pp. 14–26.

[37] G. LIU, M. CHEN AND M. LI, *Lower bound of vibration modes using the node-based smoothed finite element method (NS-FEM),* Int. J. Comput. Methods, 14 (2017), p. 1750036

[38] Y. WANG, J. YUE, M. LI AND R. NIU, *A stable node-based smoothed finite element method with PML technique for the elastic wave obstacle scattering,* Eng. Anal. Bound. Elem., 130 (2021), pp. 249–267.

[39] G. LIU, *A novel pick-out theory and technique for constructing the smoothed derivatives of functions for numerical methods,* Int. J. Comput. Methods, 15 (2018), p. 1850070.

[40] Y. LI AND J. YUE, *Contact analysis based on a linear strain node-based smoothed finite element method with linear complementarity formulations,* Int. J. Comput. Methods, (2021), p. 2141008.

[41] Y. LI AND G. LIU, *A novel node-based smoothed finite element method with linear strain fields for static, free and forced vibration analyses of solids,* Appl. Math. Comput., 352 (2019), pp. 30–58.

[42] J. YUE, M. LI AND P. LI ET AL., *Numerical solution of an inverse obstacle scattering problem for elastic wave,* Commun. Comput. Phys., 26 (2019), pp. 809–837.

[43] J. LIGGETT, *Exact formulae for areas, volumes and moments of polygons and polyhedra,* Commun. Appl. Numer. Methods, 4 (1988), pp. 815–820.

[44] W. CHEW, J. JIN AND E. MICHIELSSEN, *Complex coordinate stretching as a generalized absorbing boundary condition,* Microwave Opt. Tech. Lett., 15 (1997).